A CORRECTION FOR EMITTANCE-MEASUREMENT ERRORS CAUSED BY FINITE SLIT AND COLLECTOR WIDTHS*

R. C. Connolly,† K. F. Johnson, and V. Yuan
Accelerator Technology Division
Los Alamos National Laboratory
Los Alamos, NM 87545

Abstract

One method of measuring the transverse phase-space distribution of a particle beam is to intercept the beam with a slit and measure the angular distribution of the beam passing through the slit using a parallel-strip collector. Together the finite widths of the slit and each collector strip form an acceptance window in phase space whose size and orientation are determined by the slit width, the strip width, and the slit-collector distance. If a beam is measured using a detector with a finite-size phase-space window, the measured distribution is different from the true distribution. The calculated emittance is larger than the true emittance, and the error depends both on the dimensions of the detector and on the Courant-Snyder parameters of the beam. Specifically, the error gets larger as the beam drifts farther from a waist. This can be important for measurements made on high-brightness beams, since power density considerations require that the beam be intercepted far from a waist. In this paper we calculate the measurement error and we show how the calculated emittance and Courant-Snyder parameters can be corrected for the effects of finite sizes of slit and collector.

Introduction

When the transverse phase space of a beam is measured by scanning the beam with a slit and measuring the angular distribution of the beam passing through the slit with a parallel-channel collector, the measured distribution is the convolution of the true distribution with the acceptance window of the detector. The beam emittance and its Courant-Snyder parameters determined from the measured distribution are different from the true values.

The error caused by the slit-gap width was calculated by Gluckstern [1]. In this paper we extend his calculation to include the error caused by finite-width collector strips.

The next section of this paper calculates the error. Then the size of the effect is evaluated as a function of the slit and collector widths and the slit-collector drift distance for a beam measurement which has been reported [2]. Finally we show how the true beam parameters can be determined from the measured data.

Measurement Theory

The problem is illustrated in Fig. 1. A collector with conducting strips 2e wide is placed a distance L from a slit of width 2b. The slit is positioned a distance X_i from the beam axis (X_o, X'_o) and the centers of the slit and collector strip define a trajectory inclined at an angle X'_i with respect to the beam axis. In the configuration of Fig. 1, the slit and collector have the phase-space acceptance shown in Fig. 2.

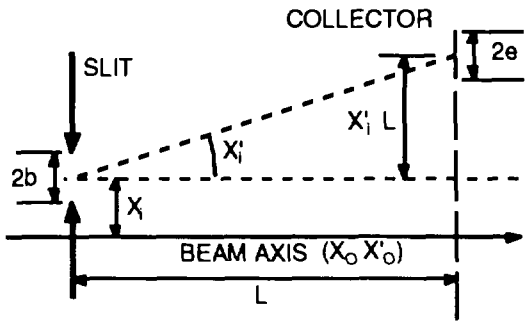

Fig. 1. Geometry of slit-collector detector.

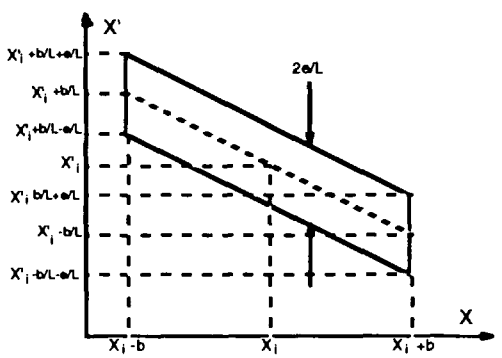

Fig. 2. Phase-space acceptance of slit and collector strip.

The beam to be measured has a true phase-space density distribution of $\rho(X,X')$. When this beam is measured with the slit and collector in Fig. 1, the measured distribution is

$$\rho_m(X_i,X'_i) = \frac{L}{4be}\iint \rho(X,X')\,dX\,dX' \quad , \tag{1}$$

where the integral is over the parallelogram-shaped phase window in Fig. 2. If $\rho(X,X')$ is expanded to second order in a Taylor series and substituted into Eq. 1, the result of the integration is

$$\rho_m(X_i,X'_i)=\rho(X_i,X'_i) + \frac{b^2}{6}\left(\frac{\partial^2\rho}{\partial X^2}\right)_{Xi,X'i} + \frac{e^2+b^2}{6L^2}\left(\frac{\partial^2\rho}{\partial X'^2}\right)_{Xi,X'i} - \frac{b^2}{3L}\left(\frac{\partial^2\rho}{\partial X\partial X'}\right)_{Xi,X'i} . \tag{2}$$

The rms emittance of a beam is defined as

*Work supported and funded by the US Department of Defense, Army Strategic Defense Command, under the auspices of the US Department of Energy.

† Industrial partner, Grumman Space and Electronics Division.

$$E = \pi \left[\langle (X-X_o)^2 \rangle \langle (X'-X'_o)^2 \rangle - \langle (X-X_o)(X'-X'_o) \rangle \right]^{1/2} \quad (3)$$

where

$$\langle (X-X_o)^2 \rangle = \frac{\int\int (X-X_o)^2 \rho(X,X')\,dX\,dX'}{\int\int \rho(X,X')\,dX\,dX'} \quad (4)$$

with similar expressions for $\langle (X'-X'_o)^2 \rangle$ and $\langle (X-X_o)(X'-X'_o) \rangle$.

The apparent emittance from a beam measurement is found by using the distribution given by Eq. 2 in Eq. 3. If the beam is symmetric about (X_o,X'_o), and the lowest-order terms are kept, the apparent emittance is,

$$(E)_m^2 = E^2 + \frac{b^2}{3}\left[\frac{\langle (X-X_o)^2 \rangle}{L^2}\left(1 + \frac{e^2}{b^2}\right) + \langle (X'-X'_o)^2 \rangle + \frac{2\langle (X-X_o)(X'-X'_o) \rangle}{L} \right] \quad (5)$$

The measured emittance is larger than the true beam emittance. For a given beam the error increases as b or e become larger or as L becomes shorter. If the geometry of the slit-collector detector is fixed, the error increases as the drift distance from a waist is increased. As a beam drifts both $\langle X^2 \rangle$ and $\langle XX' \rangle$ get larger.

The formalism outlined above can be put into a useful form by the use of the Courant-Snyder parameters defined as

$$\beta = \frac{\pi \langle (X-X_o)^2 \rangle}{E} \quad \gamma = \frac{\pi \langle (X'-X_o')^2 \rangle}{E} \quad \alpha = -\frac{\pi \langle (X-X_o)(X'-X_o') \rangle}{E}.$$

Equation 5 becomes

$$(E)_m = E\left(1 + \frac{\Delta}{E}\right)^{1/2} \quad (6)$$

where,

$$\Delta = \frac{\pi b^2}{3}\left(\frac{\beta}{L^2}\left(1 + \frac{e^2}{b^2}\right) + \gamma - \frac{2\alpha}{L} \right) \quad (7)$$

To apply Eq. 6 to the design of a slit and collector system, it is convenient to consider the dimensions of the measured beam at the last waist. When the phase ellipse is upright, it has an rms extent along X of A and along X' of θ. The emittance and Courant-Snyder parameters at the waist are $E = \pi A\theta$, $\beta(0) = \frac{A}{\theta}$, $\gamma(0) = \frac{\theta}{A}$, and $\alpha(0) = 0$. If a measurement is made a distance Z downstream from this waist the C-S parameters are

$$\beta(Z) = \beta(0) + Z^2\gamma(0) \quad \alpha(Z) = -Z\gamma(0) \quad \gamma(Z) = \gamma(0). \quad (8)$$

Equations 8 can be substituted into Eqs. 7 and 6 to give

$$E_m = E\left(1 + \frac{1}{3}\left(\frac{b^2}{A^2} + \frac{b^2+e^2}{L^2\theta^2} + Z\left(\frac{2b^2}{LA^2}\right) + Z^2\left(\frac{b^2+e^2}{L^2A^2}\right)\right)\right)^{1/2}. \quad (9)$$

Application of Measurement Theory

We previously reported a transverse phase-space measurement made on the accelerator test stand at Los Alamos National Laboratory [2]. The proton beam had rms dimensions of ~0.32 mm and ~5.8 mrad at the waist and the measurement was made ~235 mm beyond the waist. The slit and collector were spaced 625 mm apart and their half widths were; slit = b = 0.05 mm and collector = e = 0.25 mm. Using these values, Eq. 9 estimates that the emittance calculated from the measurement was 2.1% larger than the true emittance. The actual error is calculated from the measured beam parameters in the next section.

Figure 3 plots contours of constant measurement error on the (e,b) plane for the specific beam and slit-collector spacing given above. The concave-down contours give (e,b) combinations which produce measurement errors of 2, 4, 6, 8, and 10%. The acceptance window shown in Fig. 2 has an area of 4eb/L so, for a given L, the size of the measured signal is proportional to the product eb. The concave-up contours are those for which the product eb is constant. Combinations of e and b which fall on the diagonal line produce the largest signal for a given measurement error. The circle represents the slit and collector combination we used for our measurement.

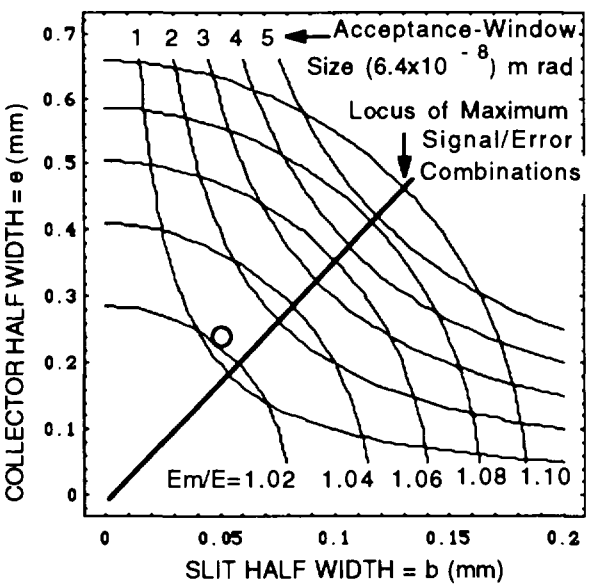

Fig. 3. Contours of constant measurement errors and constant signal sizes on the e,b plane.

The effect of the slit-collector spacing on the measurement error is shown in Fig. 4. This is E_m/E plotted as a function of L with all the parameters except L set equal to their actual values. The dotted lines indicate the drift distance and error of the actual measurement. Since the signal size is proportional to L^{-1}, a shorter spacing of 420

mm would have increased the signal by 50% and would have doubled the error.

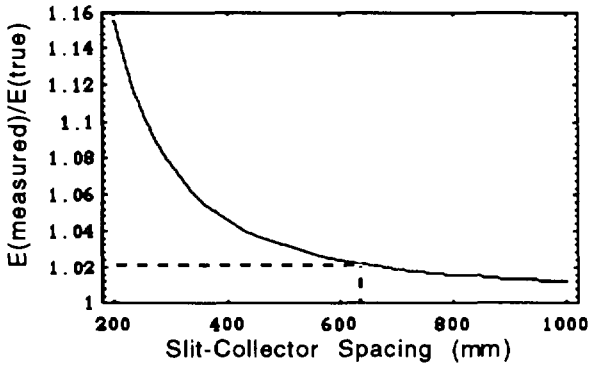

Fig. 4. Measurement error vs. slit-collector spacing.

In Fig. 5 the measurement error is plotted as a function of the slit distance from the waist. Using the same detector, the error would have been 1% at 100 mm and 5% at 400 mm.

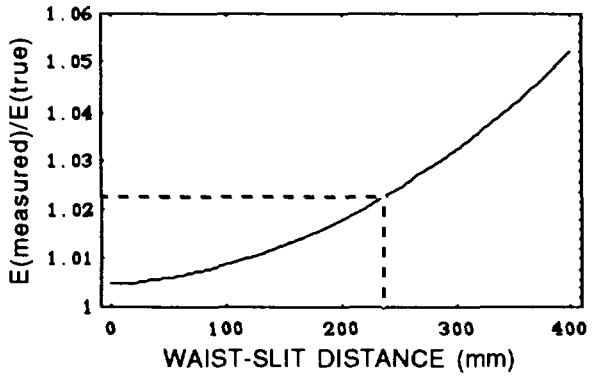

Fig. 5. Measurement error vs. beam waist-slit spacing.

Correcting Emittance Measurements

After a measurement has been made and the emittance and Courant-Snyder parameters have been calculated from the second moments of the distribution, the effect of the slit-collector error can be evaluated and corrected. The emittance correction is

$$E = E_m \left(1 - \frac{\Delta_m}{E_m} \right)^{1/2},$$

$$\Delta_m = \frac{\pi b^2}{3} \left(\frac{\beta_m}{L^2} \left(1 + \frac{e^2}{b^2} \right) + \gamma_m - \frac{2\alpha_m}{L} \right) \tag{10}$$

where the subscripts m indicate values calculated from the measured distribution. In making this correction the uncertainty of the calculated true emittance value is larger than the uncertainty of the measured emittance. If the measurement gives a value of $E_m \pm \Delta E_m$, then the true value is $E \pm \Delta E$, where

$$\Delta E = \Delta E_m \left(1 + \frac{\Delta_m^2}{4E_m(E_m - \Delta_m)} \right)^{1/2}. \tag{11}$$

After the true emittance has been calculated, the Courant-Snyder parameters can be corrected by using

$$\beta = \beta_m \frac{E_m}{E} - \frac{\pi b^2}{3E} \quad \alpha = \alpha_m \frac{E_m}{E} - \frac{\pi b^2}{3LE} \quad \gamma = \gamma_m \frac{E_m}{E} - \frac{\pi b^2 (e^2 + b^2)}{3L^2 E}. \tag{12}$$

The beam measurement reported in [2] has been corrected using these equations. The results are

Parameter	Measured	Corrected
Emittance	$(1.93 \pm 0.02) \times 10^{-4}$ π m rad	$(1.87 \pm 0.02) \times 10^{-4}$
α	-5.22	-5.38
β	1.55 m	1.60 m
γ	18.2 m^{-1}	18.7 m^{-1}

Conclusion

We have calculated the error caused by the finite sizes of the slit and collector in emittance measurements. These results can be used to design a system which is appropriate for the beam to be measured. An example was given from one of our previous measurements, for which it showed a 3% error. We could have increased both the slit gap and the collector widths and decreased the slit-collector distance and kept the error under 10%. Also the slit could have been moved downstream reducing the power loading on the slit or giving more space for a deflector magnet in laser-neutralization measurements [2].

It is important for measurements using laser neutralization of H- beams to have the slit-waist distance large and to have large signals. Using the equations of the last section measurement errors can be corrected. This calculation does not consider the step sizes used in taking the data. It has been shown [3] that at least five measurements should be made across the beam section or granularity errors arise. For this reason if large slits and collectors are used they might have to stepped in increments smaller than their widths.

References

[1] R. L. Gluckstern, "Notes on Beam Dynamics in Linear Accelerators," Los Alamos National Laboratory report LA-8526-MS, pp. 48-52.

[2] R. C. Connolly, K. F. Johnson, D. P. Sandoval and V. Yuan, "A Transverse Phase-space Measurement Technique for High-brightness H⁻ Beams," Nucl. Instr. and Meth. A312 (1992) pp. 415-419.

[3] J. Guyard and M. Weiss, "Use of Beam Emittance Measurements in Matching Problems," Proc. 1976 Linear Accel. Comf., Atomic Energy of Canada Limited report AECL-5677, 254 (1976).

LOG-RATIO BEAM POSITION MONITORING AT 425 MHz*

F. D. Wells, R. E. Shafer, and J. D. Gilpatrick
Los Alamos National Laboratory, MS: H808
Los Alamos, NM 87545

Abstract

A logarithmic-ratio beam position monitoring circuit has been designed, based on a monolithic logarithmic-amplifier integrated circuit that provides 70 dB of gain over the 100-MHz to 500-MHz frequency range. Log-ratio circuits previously reported operate at frequencies below 100 MHz [1, 2, 3]. Operation at higher accelerator bunching frequencies previously required down-conversion to an intermediate frequency in the 20 to 100 MHz range. This new circuit offers the possibility of position measurement without down conversion.

Introduction

Logarithmic-ratio processing of beam position monitor (BPM) signals is currently under investigation at several Laboratories. The technique, which has been described in four publications [1, 2, 3, 4], is attractive because it provides the most linear response across the aperture of a cylindrical BPM probe as compared to difference-over-sum and amplitude-modulation to phase-modulation (AM/PM) processing [4].

The first monolithic logarithmic amplifier applied to this application was the Analog Devices Model AD640, having a frequency range of 20 to 100 MHz [1, 2, 3]. Many accelerator bunching frequencies are above this range and down conversion is required to obtain a suitable intermediate frequency below 100 MHz.

SL3522A Logarithmic Amplifier

In 1990, the Plessey Semiconductor Company introduced the SL3522A, a 70-dB logarithmic amplifier having a frequency range of 100 to 500 MHz. This device is a successive detection logarithmic/limiting, monolithic amplifier that produces a Log/Lin characteristic for input signals between +6 and -64 dBm with a linearity of ±1 dB.

Comprising the circuit are six stages of 12-dB gain each, seven detector stages, a limiting rf output buffer and a video output amplifier. For the log-ratio circuit application the rf output buffer is disabled.

Fig. 1 shows a typical transfer characteristic of an amplifier operating at 425 MHz. Ideally, the plot should be a straight line, but in reality the line deviates by about 5% from a straight line fit between -10 and -50 dBm. This compares to a 1% deviation exhibited by a typical AD640 operating at 60 MHz [1, 2]. This deviation from linearity is a principle source of error in the log-ratio application.

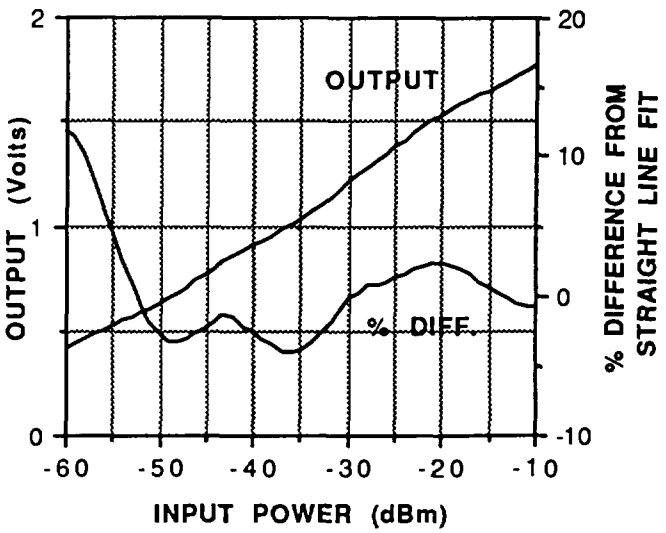

Fig. 1 Transfer curve for the SL3522A operating at 425 MHz.

The Log-Ratio Circuit

A block diagram of the log-ratio beam position monitor circuit is shown in Fig. 2. Two SL3522A amplifiers are used with their filtered outputs applied to a differencing amplifier that produces a beam-position signal proportional to log (A/B).

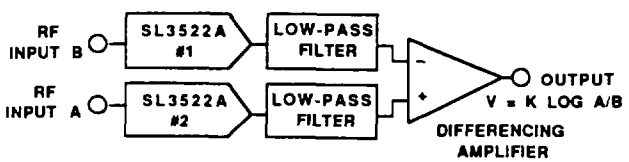

Fig. 2 The log-ratio circuit block diagram.

*Work supported and funded by the US Department of Defense, Army Strategic Defense Command, under the auspices of the US Department of Energy.

The response of this circuit to 425-MHz rf input signals is illustrated by Fig. 3. The sinusoidal variations are attributed to the successive approximation circuit technique used for achieving the logarithmic response in the amplifiers and to the deviation of the transfer curves from the ideal straight line.

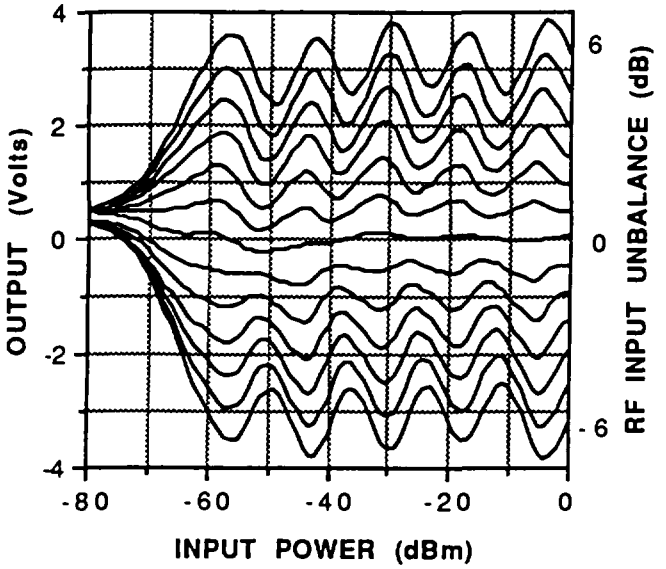

Fig. 3 Response curves of the log-ratio circuit operating at 425 MHz.

A plot of peak-to-peak error versus beam position is shown in Fig. 4 for a cylindrical probe having a subtended angle of 45 degrees. The error ranges from 2% at the center of the probe to approximately 8% at 0.2 of the probe radius.

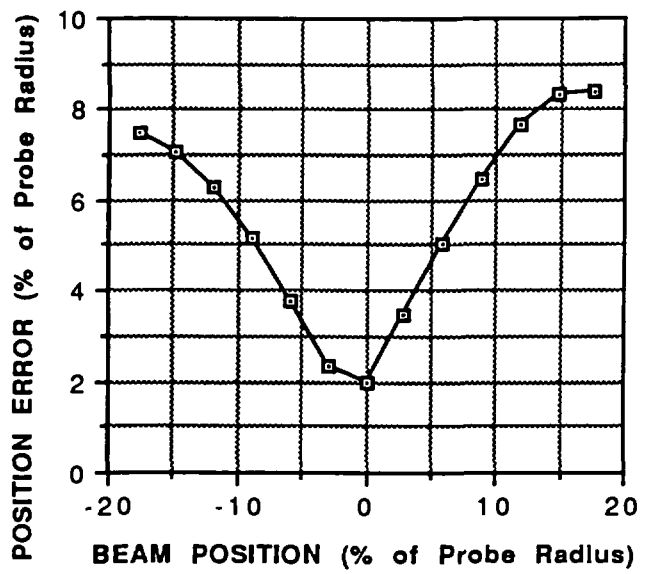

Fig. 4 Peak-to-peak error versus beam position.

Log-Ratio Compared to AM/PM Processing

An ideal system for measuring beam position should provide data that is independent of beam intensity over several decades of beam current. In general, the AM/PM system comes closest to this ideal because limiters are available that are phase matched over three or more decades of input signal voltage [5]. However, the maximum useful frequency limit is about 50 MHz. AM/PM systems operating above 100 MHz are generally limited to one or two decades of beam current and the measurements are sensitive to the beam current intensity.

Although the measurement accuracy of this log-ratio circuit is substantially worse than the AM/PM technique with down conversion, the device is usable at 425 MHz and it operates over six decades of rf-input power. AM/PM circuits are essentially unusable for this frequency and power range. The log-ratio technique is immediately adaptable to beam centering applications and the cost is about one-fifth that of AM/PM equipment. Log-ratio processing will become more viable as improved logarithmic amplifiers are designed by the semiconductor industry.

REFERENCES

[1] F. D. Wells, R. E. Shafer, J. D. Gilpatrick and R. B. Shurter, "Log-Ratio Circuit for Beam Position Monitoring," AIP Conference Proceedings 229, Accelerator Instrumentation, pp. 308-314, 1990.

[2] F. D. Wells, R. E. Shafer, J. D. Gilpatrick and R. B. Shurter, "Log-Ratio Circuit for Beam Position Monitoring," Conference Record of the 1991 IEEE Particle Accelerator Conference, pp. 1139-1141.

[3] G. R. Aiello and M. R. Mills, "Beam Position Monitor Electronics Using DC Coupled Demodulating Logarithmic Amplifiers," European Particle Accelerator Conference Record, 1992.

[4] R. E. Shafer, "Beam Position Monitoring," AIP Conference Proceedings 212, Accelerator Instrumentation, p. 47, 1989.

[5] F. D. Wells and S. P. Jachim, "A Technique for Improving the Accuracy and Dynamic Range of Beam Position-Detection Equipment," Proceedings of the 1989 IEEE Particle Accelerator Conference, pp. 1595-1596.

USE OF AN INR-STYLE BUNCH-LENGTH DETECTOR IN THE FERMILAB LINAC

Elliott S. McCrory and Charles W. Schmidt
Fermi National Accelerator Laboratory*
Batavia, IL 60510, USA

CA9700241

A. V. Feschenko
Institute for Nuclear Reasearch of the Russian Academy of Sciences
Moscow, 117312, Russia

ABSTRACT

A device to accurately measure the phase extent of a linac beam is being developed for use in the Fermilab 400 MeV Linac Upgrade [1]. Prototypes have been and are being tested. We have attempted to improve the original design from the Institute for Nuclear Research in Moscow (INR) [2] to increase the resolution for adequate operation at 805 MHz. The device incorporating a new arrangement of lens and deflector, reported previously [3], cannot achieve the desired resolution.

This paper describes the operation and the strengths and weaknesses of the three types of bunch-length detectors (BLDs) and the measurements made at this time. The differences among these devices is delineated by the relative position of the rf deflector and the electrostatic einsel lens, as follows:

INR	Lens before deflector	Figure 1
Fermilab	Lens after deflector; H- beam	Figure 2
FNAL/INR	Lens and deflector combined	Figure 3

To satisfy the goals of commissioning the new linac, a resolution of about 5 picoseconds (1° at 805 MHz) is desired.

PRINCIPLE OF OPERATION

Referring to the reference [4] and to Figure 1, an INR BLD works as follows. The primary ion beam impinges on a retractable wire target, **1**, which is at negative high voltage, V≈-10kV, wire ∅=125 μm. The passage of the beam through the wire causes secondary electrons to be liberated from the atoms in the wire. Free secondary electrons near the surface migrate out of the wire and are accelerated radially away from it by the voltage, V, to the collimator, **2**. An electrostatic einsel lens, **3**, then focuses the electrons onto the slit at the far end of the detector, **5**. Along the way, the electrons are deflected by the rf deflector, **4**, which oscillates with a voltage equal to $U(t) = A\cos(\omega t + \phi)$, where ω is equal to a multiple of the Linac bunching frequency and ϕ is a controllable phase angle. The transit time through the deflector is approximately π. For some initial angle ϕ, the electrons will pass through the slit, **5**, and enter the electron detector, **6**. This detector can be a faraday cup or an electron multiplier tube. Because the temporal distribution of the

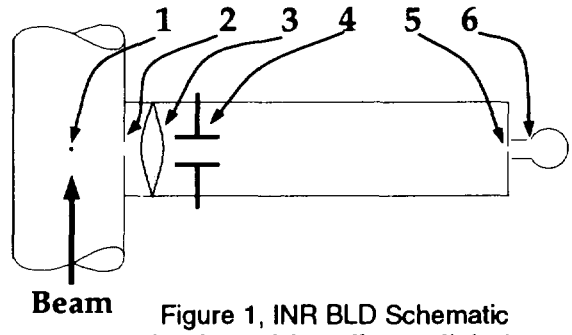

Figure 1, INR BLD Schematic

electron beam on the plane of the collector slit is determined by the deflector, not by the electron detector, the bandwidth of the electron detector is largely irrelevant. It can, in fact, be an integrator. The intensity of the signal on **6** as a function of the phase angle ϕ is equivalent to the density of the primary ion beam as a function of the bunching phase angle.

The operation of the other types of BLDs is similar. In the Fermilab device, a higher gradient is necessary in order to compensate for the focussing of the lens. The electron beam line is tuned off-line by using thermionically emitted electrons emitted from the wire when it is heated by a current (for us, 1 to 2 A at 60Hz).

RESOLUTION OF THE DETECTORS

Several significant factors determine the resolution of these devices. Four major effects are considered here

The first factor is the time necessary for the secondary electrons to be ejected from the wire. This time has been measured [5] at <6 ps, or 1.74° at the bunching frequency of the Fermilab 400 MeV Linac, 805 MHz.

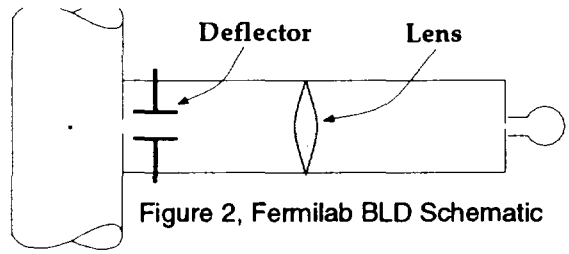

Figure 2, Fermilab BLD Schematic

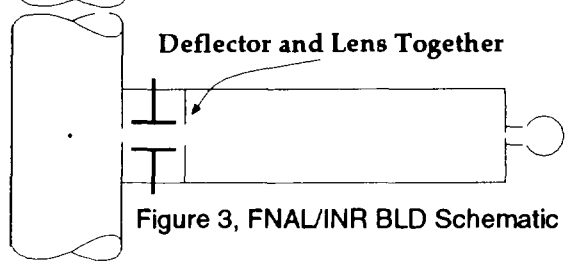

Figure 3, FNAL/INR BLD Schematic

* Fermilab is operated by the Universities Research Association under contract to the US Department of Energy.

The second factor is the emittance of the secondary electron beam. A velocity spread arises from the thermal velocities of the secondary electrons before they are ejected from the wire. The resolution here is proportional to d/V^2 where d is the drift from the target to the deflector and V is the voltage on the target. It is possible to reduce this effect to about 1 ps by shortening the drift distance and by using 10 kV on the target. The transverse emittance has essentially no effect on the resolution.

The third effect is the path-length differences among the electrons and is determined by the optics of the electron beamline. Those electrons which travel away from the center line of the detector take longer to reach the deflector than the electrons which travel on the axis of the device. This effect is likewise proportional to the drift from the target to the deflector. Also, if the lens is farther away from the target (decreasing the magnification of the image and reducing the spread of the beam), this effect is also reduced. Again, using a higher voltage and a shorter drift, this effect reduces the resolution by only about about 0.5 ps.

The fourth effect is the strength of the rf deflector. A stronger deflection, to first order, will increase the resolution. For a deflection which is too large, part of the electron beam hits the deflecting plates for any ϕ. Also, the fringing fields become more important. For the INR detector, a gradient of about 100 V/cm is optimum and good resolution is obtained (6 ps, or 0.4° at 198 MHz). For the Fermilab-type detector, it was thought that 5000 V/cm would be necessary to increase the resolution to below 5 ps, or 1° at 805 MHz.

A summary of these effects is presented in Table 1. Note that the INR detector was designed for a bunching frequency of 198 MHz with the deflector running at 594 MHz, whereas the other two are for 805 MHz. The total resolution for the INR detector is measured; for the other two, it is estimated.

Table 1.

Resolution of the Various BLDs

	INR	*Fermilab*	*INR/FNAL*
1	<6 ps	<6 ps	<6 ps
2	3.0	1.0	1.0
3	1.5	0.5	0.5
4	5.5	30?	6.0
Total	14 ps	30 ps?	6 to 10 ps
	(1° @ 198 MHz)	(6°? @ 805 MHz)	(1° to 1.8°)

Non-linear effects (space charge, lens aberrations) are not directly considered here. It is felt that these effect do not contribute significantly to the resolution of the device.

DEVELOPMENT OF THE FERMILAB DETECTOR

It was decided we would build a Fermilab-type detector for prototyping at 200 MeV. The device (Figure 2)

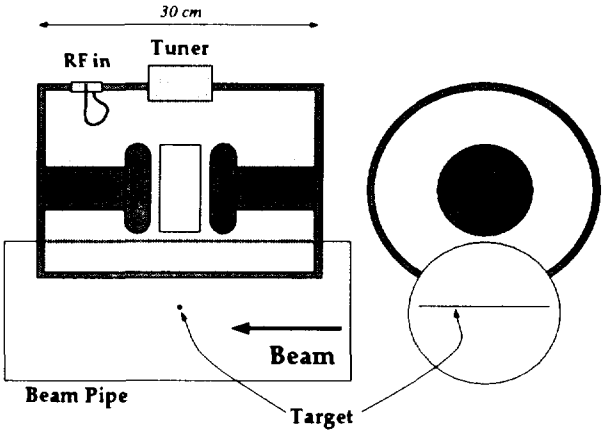

Figure 4, Schematic of the Fermilab Deflector

requires substantial power in the rf deflector. A suitable deflector has been fabricated, shown in Figure 4. We have applied 200 W to this cavity for a gradient of 5000 V/cm across its 3 cm gap. The interior of the deflector was coated with a thin (150 Angstrom) layer of titanium nitride to increase the limit for multipactoring.

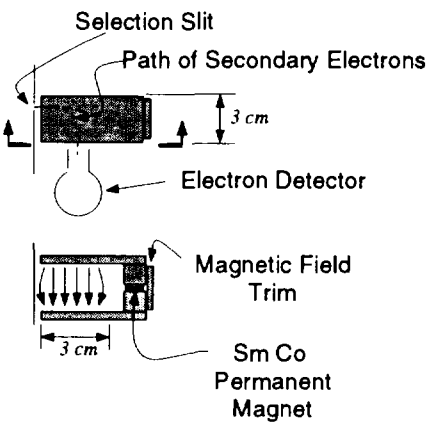

Figure 5, Selection Magnet

In order to reject the primary electrons scattered off the wire from our H- beam, it is necessary to install a permanent-magnet deflector (Figure 5) between the selection slit and the electron detector. The energy of the scattered electrons which would pass into our detector is several hundred keV, so rejecting these electrons is easy. The permanent magnet used in this deflector is a samarium-cobalt magnet with a surface field of approximately 8000 Gauss. The field in the bending region has been trimmed to a value of about 133 Gauss, which corresponds to ρ=2.54 cm for 10 keV electrons.

We have discovered two debilitating problems with this style of detector. (1) The electrons from the secondary electron beam will induce multipactoring at a power level no greater than 700 V/cm for our 3 cm gap. That threshold is reduced if electrons hit the inside of the rf chamber. This means we cannot achieve adequate gradient in the cavity to produce a satisfactory resolution. (2) The trajectory which passes through the first and the last collimator slits (and through the rf deflector) does not pass through the axis of the einsel lens. Thus, the einsel lens must have a relatively large aperture, larger than one would expect for an abberation-free lens. Moreover, this trajectory also exits from the rf deflector considerably off axis which may induce multipactoring.

We will not pursue this design further.

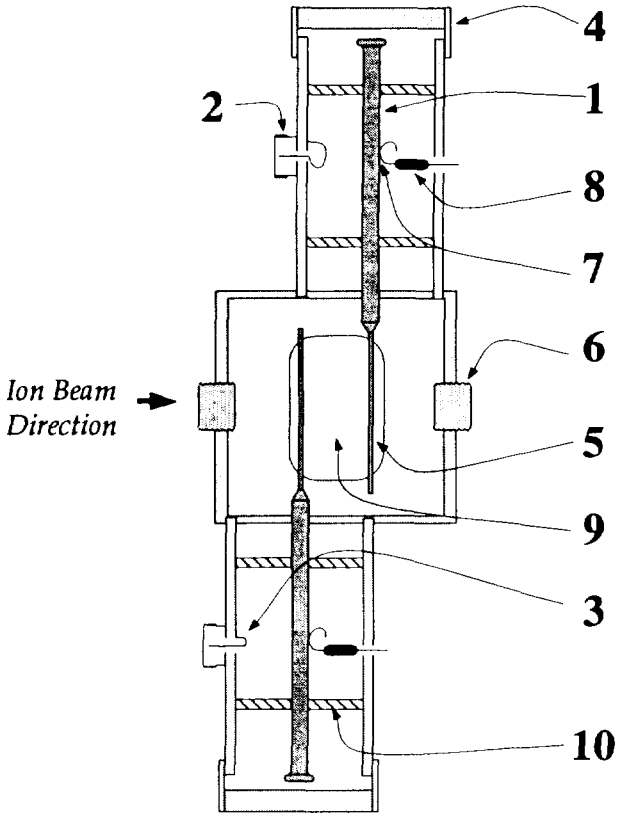

Figure 6, Deflector Schematic for FNAL/INR BLD

THE FNAL/INR DETECTOR

A BLD with the best features of the other two has been developed. It combines the deflector and the einsel lens into a single unit. This arrangement has several benefits. It allows the deflector to be placed very close to the target, as in the Fermilab detector. Also, since the rf deflector plates have a negative DC potential applied to them for the lens, multipactoring should not occur.

The design of the deflector/lens is as follows (refer to Figure 6): Each of the two arms of the deflector form a resonant coaxial cavity, **1**; the length of each arm is $\lambda/2$ at our frequency of 805 MHz. One coupling loop provides the input rf power, **2**, and the other loop provides the readback, **3**. The resonant frequency of the two arms of the deflector is tuned by adjusting the end-caps, **4**, and by trimming the size of the deflector plates, **5**. Small slug tuners, **6**, provide the final trimming to the desired resonant frequency.

The DC voltage for the lens is applied near the point of zero rf field along the center conductor of the coaxial arms, **7**, at the $\lambda/4$ point of each resonator through a 1 MΩ resistor, **8**. Secondary electrons pass through the input slit and are deflected and focussed in the central region of the deflector, **9**, and exit through the rear of the rf chamber. The exit aperture is large enough not t intercept any beam. The arms are supported by nylon rings, **10**. The equivalent impedance $R_{eq} = U_{max}^2/2P$ is measured to be 90 000 Ω, where U_{max} is the maximum rf voltage between the deflector plates and P is the dissipated power.

The optimum deflecting gradient for this deflector has been estimated by computer simulation. The electric field in the deflector is calculated as a superposition of the electrostatic focusing field and the rf deflecting field using a quasi-static approximation. The field distribution is considered to be flat. The distribution of the electrostatic fields in the deflector chamber is taken to be the same as for a coaxial line and has been calculated analytically.

A delta-function incident ion beam is assumed and the size of the secondary electron image on the final selection sit is calculated. The resolution here is defined to be

$$\Delta\Phi = 2\sigma_e/X_{max},$$

where σ_e is the size of the electron beam at the detector slit and X_{max} is the maximum deflection on the plane of the detector slit caused by the rf deflector. 200 electrons are used in the simulation for the calculation of each point. The results are presented in Figure 7. It is interesting to note that the increase in the size of the electron beam is approximately cancelled for by the increasing amplitude of its deflection.

The deflector has been tested in vacuum. To obtain U_{max}=1000 V, 5.6 W of rf power is required.

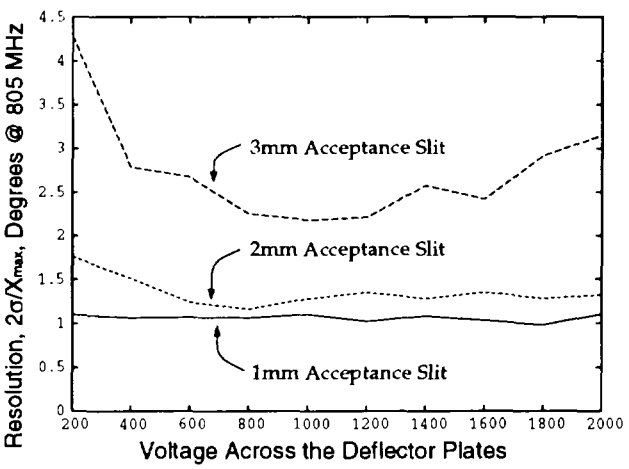

Figure 7, FNAL/INR BLD Resolution for various input collimators.

REFERENCES

[1] Robert J. Noble, "The 400 MeV Linac Upgrade at Fermilab," this conference, TH1-01.

[2] A.V. Feschenko and P.N. Ostroumov, "Bunch Shape Measuring Techniques and its Application for an Ion Linac Tuning," 1986 Linac Conference Proceedings, SLAC, pp 323-327.

[3] Elliott S. McCrory, Glenn Lee and Robert C. Webber, "Diagnostics for the 400 MeV FNAL Linac," 1990 Linac Conference Proceedings, Albuquerque, pp 456-458.

[4] Elliott McCrory, "Design Considerations for a Bunch Length Monitor at the Fermilab Linac," FNAL Linac Upgrade Document number 161.

[5] *Secondary Emission*, by Bronstein and Fraiman, pp 319-326; 1968, Nauka Publishing, Moscow, in Russian.

DEVELOPMENT OF BEAM DIAGNOSTICS FOR SPring-8 LINAC

K. Yanagida, S. Suzuki, Y. Itoh, H. Yoshikawa,
A. Mizuno, T. Hori, and H.Yokomizo
JAERI-RIKEN SPring-8 Project Team
Tokai-mura, Naka-gun, Ibaraki-ken, Japan 319-11

Abstract

The preinjector of the SPring-8 linac is constructed in Tokai Establishment. Several monitors are installed in the preinjector. They are designed to measure a low current beam such as a positron beam as well as a high current beam. A wall current monitor has achieved a fast rise time of ≤300ps.

Introduction

In the electron linac, principal beam characteristics such as beam current, emittance and energy deviation are determined by the beam dynamics from the gun to the point where the beam energy is several MeV. The preinjector was constructed to examine the beam characteristics as a part of SPring-8 linac. A beam test started from August 1992. In the preinjector several monitors are installed not only to measure the beam characteristics but also to examine the performance of monitors using the electron beam. This article presents the design and the performance of these monitors.

Design of SPring-8 Linac

The injector system of SPring-8 (Super Photon ring 8 GeV) [1] is composed of a 1GeV linac and a 8GeV booster synchrotron. The positron beam is available in this system as well as the electron beam. In order to produce a positron beam, an electron/positron converter is installed in the midst of the linac. Therefore the linac consist of a 250MeV high current linac (HL), a converter and a 900MeV main linac (ML).

The beam characteristics such as an energy, an emittance, an average peak current and a microbunch length are measured at three points; at the preinjector, around the converter and at the end of ML. Table 1 shows the beam parameters for designing monitors. The positron beam must be measured after the positron converter. For R&D monitors were designed so as to detect a low current beam, even though they are used in the high current preinjector.

The preinjector includes an electron gun, two prebunchers, one buncher, focussing magnets and beam monitors (see Fig. 1) [2]. In order to measure the performance of gun the current monitors are installed at the exit of gun. The current monitors are also installed at the exit of buncher to measure transmission rate through the prebunchers and the buncher. The beam characteristics are measured at the location after the buncher where the beam is bunched and accelerated up to 9MeV. A transverse emittance is measured by the slit1 and the wire grid monitor. An energy spectrum is measured by the spectrometer that consists of the quadrupole magnets, the slit2, the bending magnet, the slit3, and the Faraday cup. To measure a microbunch length, the Cherenkov radiators are installed. The Cherenkov radiator1 is installed for the precise measurement. Profile monitors are installed at four locations for the beam transport.

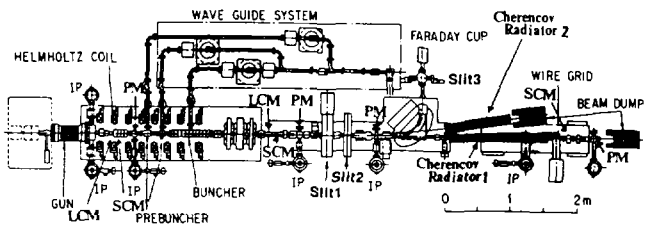

Fig. 1 Arrangement of the preinjector.

TABLE 1
Parameters for Beam Diagnostics

Pulse Width and	1	ns,	10	A
Average Peak Current	1	ns	10	mA
	10~40	ns,	10	A
	10~40	ns	10	mA
	1	ns,	300	mA
	≥1	μs,	100	mA
Microbunch Length	≥5	ps		
Beam Energy	9	MeV		for Preinjector
	250	MeV		before Converter
	120	MeV		after Converter
	1	GeV		for ML
Transverse Emittance	~10	πmm•mrad		for Preinjector
	1	πmm•mrad		for Others

Design of Monitors

This section describes the designs of each monitor, such as design parameters, a structure, an electronic circuit and so on.

Long Pulse Current Monitor (LCM)

The LCM is a monitor to measure the average peak current and the pulse width of the long pulse beam (~1μs). The required parameters are as follows; output of ≥1V/A, maximum peak current of ≥1A, rise time of ≤20ns and droop of ≤1%/μs. The model 2100 (Pearson) satisfies the parameters.

Short Pulse Current Monitor (SCM)

The SCM is a monitor to measure the average peak current and the pulse width of the short pulse beam (1~40ns). The required parameter are as follows; output of ≥1V/A,

maximum peak current of ≥10A, rise time of ≤300ps (if possible 100ps), droop of ≤10%/100ns. Two types of SCM were manufactured in order to obtain fast rise time.

One is a wall current monitor (see Fig. 2). It is composed of a ring-type ceramic resister (ASW, Tokai) with a resistance of 1.8Ω connected across the ceramic insertion, a signal pick up and a loading core (FT-1M, Hitachi).

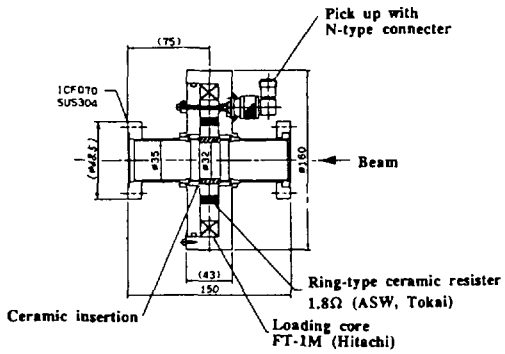

Fig. 2 Cross section of the wall current monitor.

Another is an amorphous CT (Current Transformer) (see Fig. 3). It is composed of an amorphous core (FT-1L, Hitachi) with 13 turns windings, and a signal pick up. The windings and the pick up are connected directly.

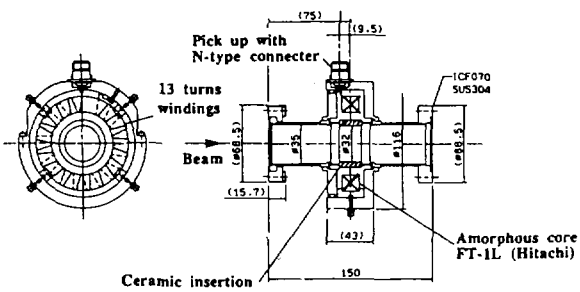

Fig. 3 Cross section of the amorphous CT.

Transverse Emittance Monitor

Two different methods [3] are introduced in SPring-8 linac for the transverse emittance measurement.

One is a method using a slit and a wire grid monitor. The phase space is scanned directly. The width and thickness of the slit are 0.3mm and 30mm respectively. The wire grid monitor has a single wire with a diameter of 0.3mm for the charge detection. And it also has two wires to extract secondary emission.

Another is a method using the three profile monitors (wire grid moitors). This method will be used in the higher energy region. Three profiles measured in the different points provides the twiss parameters and the emittance.

A charge sensitive amplifier is prepared for the signal processing. An expected charge is 1pC~0.1μC/pulse. A sensitivity is required as 1V/pC in the smallest range. At present the model 142A and 113 (Ortec) is used as the amplifier. Another charge sensitive amplifier (see Fig. 4) is developed. If it presents a good performance the multi-wire type monitor (~10 wires) and the integrated type amplifier will be used .

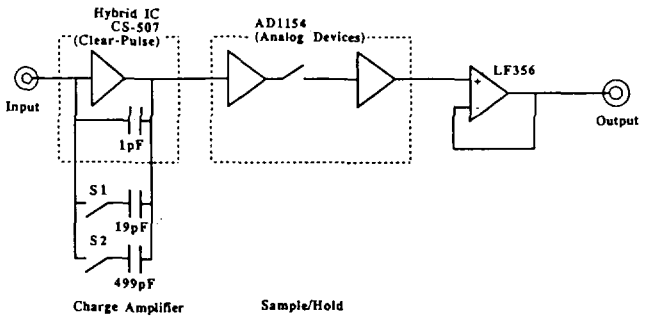

Fig. 4 Block diagram of the charge sensitive amplifier with the hybrid IC.

Microbunch Length Monitor

In order to measure the microbunch length with the smallest error the observation of Cherenkov radiation by the streak camera is preferable. Synchrotron radiation is also available but the measurement error becomes large. When the beam is bended, a geometrical bunch lengthening occurs. The bunch lengthening (Δz) is a product of beam size (Δx) and bending angle (θ).;

$$\Delta z = \Delta x \cdot \theta \qquad (1)$$

For example Δz is 0.7mm (2.3ps) where Δx=5mm and θ=0.14rad. Therefore the Cherenkov radiator1 is prepared on the straight line of the beam duct as shown in Fig. 1. In the case of the machine study, the air is filled in the radiator1 and the Cherenkov light is measured through the beam axis. However, it is unable to use the radiator1 in the normal operation because the vacuum vent is required in the beam duct, so that the Cherenkov radiator2 is prepared on the line with the bending angle of 0.14rad to the beam axis.

The Cherenkov light is transported out of the accelerator room and focused on the slit of streak camera. The focusing elements are composed of mirrors because chromatic effect is small in the case of mirrors compared with the lenses. The chromatic effect causes time error of 1ps when the light (wavelength; 250~750nm) is transported for 12m. The focusing element is a type of the Newtonian telescope (see Fig. 5). Its diameter is 150mm. The focal lengths from the elliptical mirror are 1m and 11m. In order to reduce the shadow of submirror the elliptical mirror has 75mm off set from the symmetric axis.

The streak camera is C3735-01 (Hamamatsu). Its time resolution is 0.6ps originally. It has a sufficient sensitivity to the Cherenkov radiation of the positron beam.

Total error in this measurement becomes 1.6ps (minimum) and ~4ps (beam bended).

Energy Monitor

The absolute beam energy and the energy spread is measured by the spectrometer in the preinjector. The slit2 and slit3 is located on the double waists of the beam. The

slit3 determines the energy spread and the Faraday cup measures the beam current passed through the slit3.

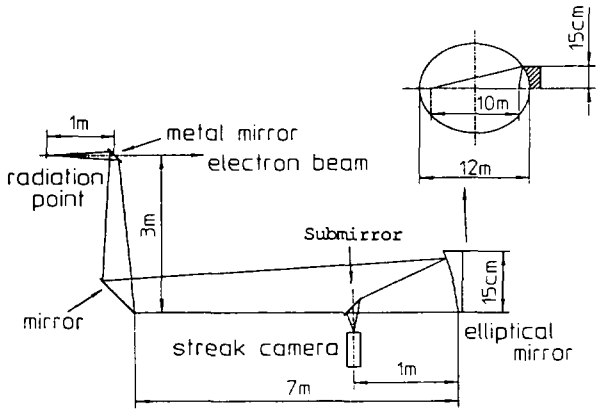

Fig. 5 Arrangement of microbunch length monitor.

Profile Monitor(PM)

This monitor is prepared for the beam transport. The PM has a scintillator screen, AF995R 1mm thickness (Desmarquest), and the profile is observed by the TV camera. The screen center is aligned to the beam axis within 0.3mm accuracy.

Present Status

The fabrication of the beam monitors for the preinjector are completed. The individual beam diagnostics show the good performance. The examination of beam monitors using the electron beam is under way. This section describes the off beam test of SCM (see Fig. 6). A pulse current transmits through the conductor instead of the electron beam. The waveform of output and transmission are measured by the sampling oscilloscope.

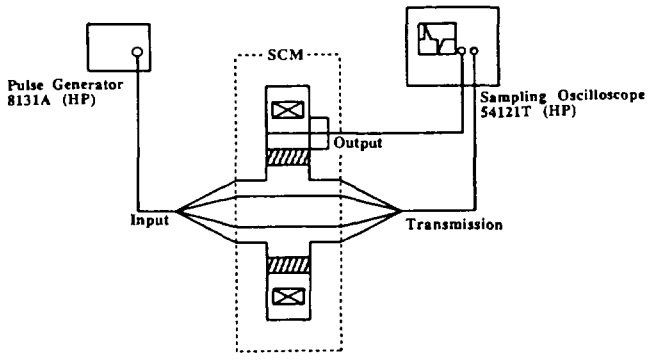

Fig. 6 Arrangement of the off beam test.

Fig. 7 shows the waveform from the wall current monitor; upper one is transmission and lower one is output. Both waveforms shows fast rise time of ~300ps which is thought to be the limit of pulse generator. The measurement of frequency spectrum indicates the upper cut off frequency of ~2GHz. Thus the rise time is expected as 170~300ps.

Fig. 8 shows the waveform from output of the amorphous CT. The deformation due to ringing is very large compare with wall current monitor's. Table 2. is the specification of SCM obtained from the test.

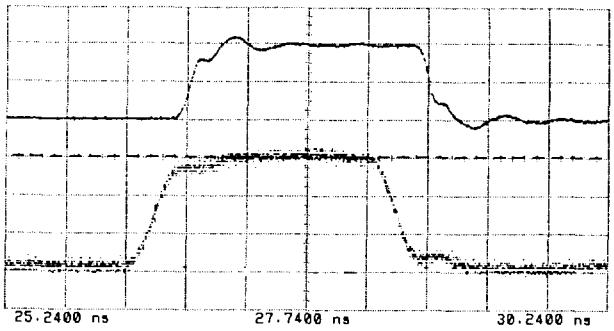

Fig. 7 Waveform from the wall current monitor. (500ps/div)
Upper: transmission (500mV/div)
Lower: output (10mV/div)

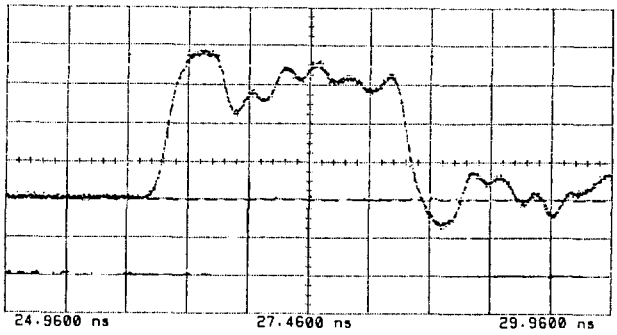

Fig. 8 Waveform from the output of the amorphous CT. (500ps/div, 20mV/div)

TABLE 2
Specification of SCM

Parameter	Wall Current Monitor		Amorphous CT	
Rise Time	≤300	ps	~300	ps
Droop	25	%/μs	0.7	%/μs
Output	1.4	V/A	3.8	V/A

A linear response for the large current (~10A) is not confirmed yet. In order to calibrate SCM a coaxial Faraday cup is prepared. The calibration will be done using the electron beam. The coaxial Faraday cup will measures the absolute pulse width and the absolute average peak current.

Conclusion

The monitors of the preinjector are well manufactured as the design. Especially, the fast time response is obtained in the wall current monitor without deformation of waveform.

References

[1] H. Kamitsubo, "8 GeV synchrotron radiation facility project in Japan: JAERI-RIKEN SPring-8 Project", Nucl. Instr. and Meth., **A303**,421(1991)
[2] H. Yoshikawa, et al., "Design of High Current Injector for SPring-8", Proc. of LINAC'92
[3] H. Koziol, "Beam Diagnostics",CERN 89-05,63(1989)

PULSED-LINAC SYNCHRONIZATION USING AN EMBEDDED MICRO-CONTROLLER

S.T. Craig, S.B. Alexander, M.P. Simpson†, R.J. West
AECL Research, Chalk River Laboratories
Chalk River, Ontario, K0J 1J0, CANADA

Abstract

A Master Timing Generator (MTG) was developed using a single Motorola MC68332 embedded micro-controller. The MTG produces electrical synchronization pulses that coordinate the action of all pulsed subsystems and the acquisition of pulsed data. Pulse width and delay-offset of each of the 13 output channels can be changed on-line. The MTG is interfaced with a GE Series-Six Programmable Logic Controller (PLC), which coordinates overall control of the IMPELA™ linac. Serial communications are used between the PLC and the MTG. The PLC needs only transmit data to define the pulse repetition rate, the beam pulse width, and the subsystems that should be active. The MTG determines the widths and relative delays required to achieve the requested beam pulse-width. Changes in width and repetition rate are effected using a smooth ramp to avoid power-demand transients. All MTG timing requirements are met with the current implementation, having the following characteristics: 1 Hz ≤ repetition rate ≤ 500 Hz with ±1% resolution, 12 μs ≤ width ≤ 1000 μs in 1 μs steps, and a delay-offset range of 4.5 ms in 1 μs steps.

Introduction

Pulsed linacs require synchronization of the electron gun, the HV power supply modulator, the rf drive and the data collection electronics. In the IMPELA™‡ industrial application,[1,2] the synchronization implementation must meet the potentially conflicting demands of flexibility, cost-competitiveness and operational simplicity. These demands have been met using a micro-controller that integrates a multi-channel "timing engine", a CPU, serial communications modules, as well as other processor support functions.

Synchronization of IMPELA is achieved using an MTG (Master Timing Generator) that is interfaced with an industrial PLC (Programmable Logic Controller). The MTG consists of the above-mentioned micro-controller, line drivers, and a circuit card that permits on-site, non-volatile adjustment of timing parameters.

Following an overview of timing requirements, the MTG design and operating experience are outlined.

Requirements

The MTG was developed for the 10 MeV, 50 kW (avg.) member of the IMPELA family. However, broader requirements were called for to meet the demands of future IMPELA linacs, covering 5 to 18 MeV and 20 to 250 kW (avg.). Basic requirements are:

- 1 Hz ≤ PRF ≤ 500 Hz (Pulse Repetition Frequency) with 5% or better resolution (1% achieved).
- 12 μs ≤ pulse width ≤ 1000 μs with 1 μs resolution.
- pulse positioning (delay) range of ≥ 4.5 ms with 1 μs resolution.

On-line changes are possible for: PRF, pulse width, delay, and pulse enable/disable. Supervisory control is realized over a serial communications link, using the CCM* protocol. A set of switches provides in-field timing adjustment by unskilled operators.

Nine separate timing signals are required. Most are required in two locations, thereby requiring fan-out. In addition, an output at 10·PRF, 50% duty-factor, is provided for monitoring.

Example Pulse Sequence

Another MTG responsibility is pulse positioning as a function of beam width. The PLC command need only specify the desired beam width and PRF. The MTG must determine the required timing. Fig. 1 illustrates a long and short width case.

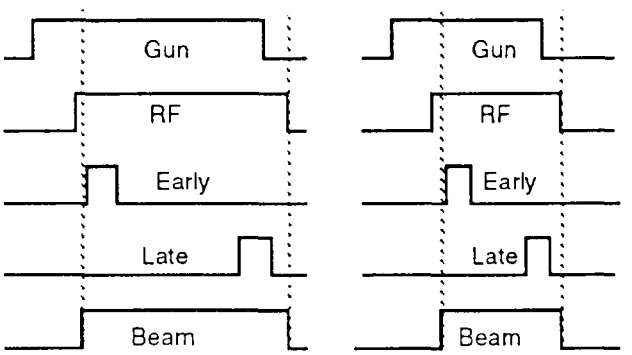

Fig. 1 Example Pulse-Timing Relationships

The gun and rf pulse widths exceed the beam width by a fixed amount. These pulses must also precede the beam by a fixed amount. The early and late pulses are data sampling triggers. The early pulse is positioned a fixed time into the beam, while the late pulse is positioned a fixed time before the end of the beam pulse.

† AECL Accelerators, Kanata, Ontario, K2K 1T9, CANADA
‡ Industrial Materials Processing Electron Linear Accelerator

* Communications Control Module protocol is a simple packet-based protocol typically used to connect a PLC with a display station or another PLC.

MC68332 Features

The development of the MC68332 was a joint effort of Motorola and Delco, the latter for automotive applications. It incorporates a 16 MHz, 32 bit CPU (68020-based), a System Integration Module[3] (SIM), serial communications hardware, a 16 channel synchronous Timing Processor Unit[4] (TPU) with 250 ns resolution and 2 kB of on-chip RAM. In the MTG, the CPU manages the serial link with the PLC. It interprets the commands, then sets TPU registers appropriately. The SIM manages pin function assignment (e.g., chip select range) and support functions, such as a watchdog; hence, very little support circuitry is required.

A MC68332 "Business Card Computer" (BCC) further reduces design effort. This BCC circuit card holds a MC68332, 128 kB EPROM (with debugging monitor), 64 kB RAM, serial drivers, clock circuitry, and two 64-pin connectors/headers. The BCC can be plugged into an evaluation/development system for code development, and then transferred to the target hardware. The headers permit attachment of a breakpoint computer or other debugging aid. The convenience of the BCC has been applied elsewhere in the construction of "smart" data acquisition and control electronics for a pulsed linac.[5]

MTG Structure

Hardware

A VME (3U x 84 hp x 160 mm) chassis houses the MTG cards and two power supplies. One card consists of 8 bytes of memory-mapped DIP switches, providing 16 µs width and delay adjustment to each channel. Baud rate and device identity are also set on this card.

The controller card is shown in Fig. 2. Due to the high level of integration on the BCC, the support electronics on the controller card consist simply of: RS-422 transceiver, EPROM, watchdog alarm buffering, and key-switch access to the BCC debug EPROM via a front-panel RS-232 port.

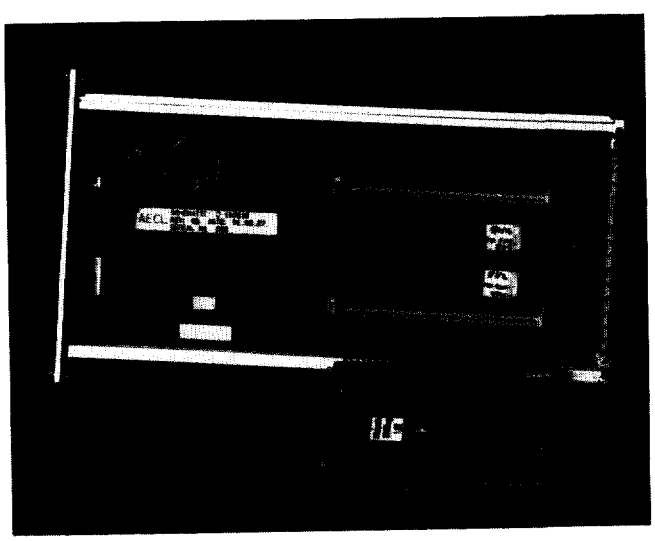

Fig. 2 Controller Card, BCC Extracted

One chassis supports eight line driver cards, delivering a total of 32 electrically-isolated, differentially-driven pulses. Any timing channel may be selected for output by appropriate jumper selection. Outputs are buffered for front-panel monitoring with an oscilloscope. A front-panel LED for each output line is also provided. These LEDs indicate whether the lines are adequately loaded, thus providing a means of broken line detection.

Timing Software

CPU The CPU code was written in 'C' language using a PC-based compiler. A skeleton of this code is shown in Fig. 3. An infinite loop services the watchdog, monitors communication activity and updates timing parameters during width or PRF ramps. Once PLC communication has been interpreted as a valid CCM packet, the command is extracted and checked against limits in PRF, width, duty factor, etc. Valid commands are used to generate a new set of timing parameters for use by the TPU.

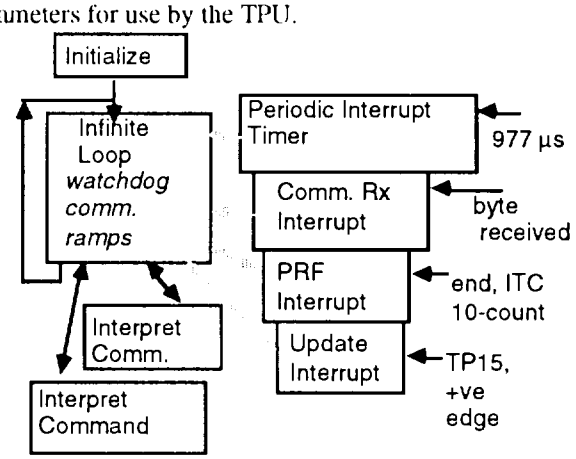

Fig. 3 Software Structure

Parameters are written into the TPU during service of TPU-generated interrupts. One TPU interrupt is used for updating the PRF and the other is used for updating the width and delay of all output channels.

Interrupt service routines are also used for each byte received from the PLC, and for an internal real-time clock that is used to time CCM protocol events.

TPU By manipulating TPU control registers, the CPU can configure a TPU channel to perform one of 16 functions programmed in TPU ROM. The ROM functions are not capable of simultaneously meeting the low PRF and 1 µs width/delay specifications. Custom TPU functions can be stored in the on-chip 2 kB RAM, which can be configured to replace TPU ROM.

A custom Synchronized One Shot (SOS) function was created by extracting the TPU ROM, using in-house programs to disassemble the code, and then manually programming the bit patterns for the SOS function in place of an unused function. The SOS function begins with a TPU-internal interrupt (link). Following a programmed delay, the voltage on the channel's

upon the cycle completes and the channel remains inactive until the next link.

Application of the 16 channels is shown in Fig. 4. A Pulse Width Modulation (PWM) function produces a 50% duty factor signal at 10·PRF. Generation of this signal is based on Timing Control Register 1 (TCR1), which increments on a 3.8141 μs interval. Two Input Transition Counters (ITC) divide the 10·PRF signal to produce links at the PRF. Two ITC channels are required, due to a link-limit of 8 channels. The first ITC interrupts the CPU on each 10-count, so that the PRF can be updated. This interrupt also notifies the CPU of each pulse trigger; thus, the CPU can implement single-pulse events.

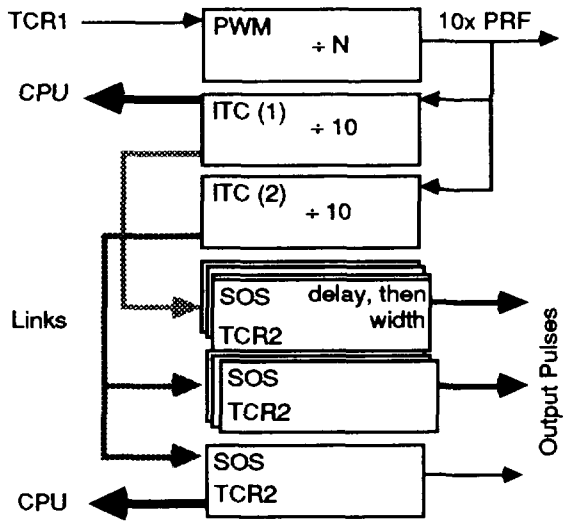

Fig. 4 TPU Configuration

SOS channels base their pulse delays and widths on TCR2, which counts on a 476.8 ns interval. The last SOS channel must be configured such that its pulse rising edge follows the rising edge of all other SOS pulses. The rising edge of this last pulse interrupts the CPU, allowing the synchronous update of all widths and delays.

Jitter between SOS channels is 80 ns. For the IMPELA 10/50, the minimum beam pulse length is 50 μs; hence, the jitter contributes < ±0.1% to beam current variability.

Communications

The MTG implements the slave portion of the CCM multidrop master-slave protocol. This protocol contains a Q (for Quick) and N (for normal) message type. The Q-message is used for status polling, while the N-message performs more substantial data transfer. The Q-message, issued typically every 100 ms, is responded to with a read-back of the current PRF and beam width. A single byte gives the operating status.

In this application, N-message transfers are limited to those originating with the PLC. The first byte of the 16 byte packet defines the command. The remaining 15 bytes carry command parameters such as PRF, width and/or a list of channels to be disabled/enabled.

The original design called for a continuous background of Q-messages, with N-messages issued only when a change was requested. It was assumed that the error detection and retransmission features of the CCM protocol would ensure reliable communication. While a reliable implementation of this design has been achieved, considerably more PLC code is required than was anticipated. One example of the problems encountered is the determination of when the MTG has received an N-message. The PLC buffer for the N-message must not be overwritten until the MTG has received the message. Despite explicit message-complete acknowledgement within the CCM protocol, no reliable means of obtaining this information was found at the PLC ladder-logic level. Hence, an additional status code was added to the Q-message response to synchronize PLC transmissions.

A simpler communications scheme is planned, whereby the PLC will maintain a setpoint area in memory that the MTG will read. The MTG then will write a complete status report back into PLC memory. PLC access to these memory areas would be asynchronous with MTG access.

Conclusions

The high degree of integration provided by the MC68332 and the BCC, coupled with the inexpensive PC-based development tools, permitted cost-effective development of a flexible, custom MTG.

An MTG has been in continuous service since 1991 August. Following the correction of subtle errors in the PLC communications code, service has been error-free. The on-line capability to adjust both pulse widths and PRF has proven useful during rf conditioning, and offers a simple means of extending the range of average beam power.

References

[1] C.B. Lawrence et al., "The IMPELA Control System", Proc. European Part. Accel. Conf. , Rome, 1988 June, pp. 1237-1239.

[2] J. Ungrin et al., "Operating Experience with the IMPELA-10/50 Industrial LINAC", Proc. Linear Accel. Conf., Albuquerque, 1990 September, pp. 587-589.

[3] MC68332 SIM User's Manual, Motorola Inc. (1989).

[4] MC68300 Family TPU User's Manual, Motorola Inc. (1990).

[5] S. Shtibu, R.W. Goodwin, E.S. McCrory, M.F. Shea, "Smart Rack Monitor for the Linac Control System", Proc. IEEE Part. Accel. Conf., San Francisco, 1991 May, pp. 1484-1486.

SCRUNCHER PHASE & AMPLITUDE CONTROL

R. A. DeHaven, C.L. Morris, R. Johnson, J. Davis, J. M. O'Donnell
Los Alamos National Laboratory
P.O. Box 1663 MS-H826
Los Alamos, New Mexico 87545

Abstract

The analog controller for phase and amplitude control of a 402.5 MHz super conducting cavity is described in this paper. The cavity is a single cell with niobium explosively bonded to a copper cavity. It is used as an energy compressor for pions at the Clinton P. Anderson Meson Physics Facility (LAMPF). The controller maintains cavity frequency to within 4 degrees in phase of the LAMPF beam frequency. Field amplitude is maintained to within 2 percent. This control is accomplished at critical coupling (Q loaded of 1 x 10^9) with the use of only a 30 watt rf amplifier for accelerating fields of 6 MV/m. The design includes the use of piezoelectric crystals for fast resonance control. Three types of control, self excited, VCO, and a reference frequency driven, were tried on this cavity and we present a comparison of their performance.

INTRODUCTION

The SCRUNCHER[1] is a single cell superconducting cavity operating at 402.5 MHz. It is constructed from a 3 mm thick copper shell with a 3 mm explosively bonded niobium layer. Liquid helium flowing in copper pipes attached to the outer copper surface cools the cavity with the boiled-off cold gas used to cool the heat shields surrounding the cavity. A 60 liter liquid helium storage dewar is installed at the top of the cavity and is used as a reservoir for the cooling pipe system. Coupling to the cavity is by a 3-in. coaxial line with a movable center conductor that allows operation at loaded Q's of 1 x 10^7 to 3.6 x 10^9. Three mechanical lead screws, each in line with a piezoelectric crystal, are mounted between one end of the cryostat and one of the beam tubes attached to the cavity. Cavity tuning is accomplished by compressing the cavity with these actuators. External mounting of the piezoelectric crystals eliminates the high voltage breakdown problem experienced in a helium atmosphere. The range of the tuner is 1.6 MHz while the piezoelectric crystals generate a tuning range of 12 kHz. Since the cavity is used to manipulate the phase space of the secondary pion beam at LAMPF, the cavity frequency must be phase locked to the beam bunching frequency of 201.25 MHz as set by the accelerator. The Pion beam represents a minuscule loading effect on the cavity allowing the operation of the cavity at high loaded-Q with a low power solid state rf amplifier. Use of the piezoelectric crystal fast tuning in concert with the high frequency mechanical resonance's, resulting from the stiff large mass copper-niobium-cavity, allow frequency control to within 4 degrees of phase at operating Q's of 1 x 10^9.

ANALOG CONTROL

A. Amplitude Control

Amplitude control for the cavity is typical. A sample of power from the cavity-transmitted-pickup-probe is detected

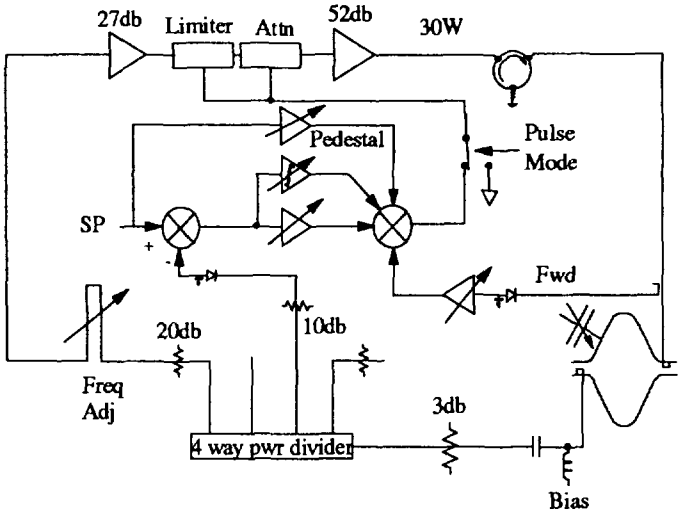

Fig 1. Amplitude Controller for Cell.

and compared to a reference voltage level (see Fig. 1). This error signal is amplified using a Proportional-Differential-Integral (PDI) controller that biases the diodes on double balanced mixers used as attenuators. These adjustable attenuators are in series with the rf drive for the final cavity amplifier. A sample of the amplifier forward output power is used for the differential state variable in the amplitude control loop. Operationally the differential input has very little effect and is not used. The pedestal is a steering signal and can be used for open loop operation of the system. Q is measured by clamping the control output to pulse the rf.

B. VCO Mode

A Voltage Controlled Oscillator (VCO) was incorporated for use in making Q measurements on the cavity. A crystal VCO operating at 201.25 MHz with frequency doublers was used because of signal to noise concerns when working with high Q. This type of oscillator has a narrow frequency range, but has the lowest noise sidebands available and worked quite

well in this application. The control loop for this system was again typical. We used a phase bridge between the oscillator output and the cavity transmitted pickup probe with a proportional controller. No attempt was made to control the absolute frequency of the cavity in this mode of operation.

C. Driven Mode

Phase Controller

This is the mode that we originally intended to operate in. A 5 kW amplifier was procured and the coupler was designed to operate the cavity overcoupled for broader bandwidth. The source of rf for the cavity amplifiers is derived by frequency doubling the 201.25 MHz from the accelerator master reference oscillator in passive doublers. The rf from the cavity transmitted pickup probe is mixed with a sample of the 402.5 MHz reference in a double balanced mixer designed to operate as a phase detector. The phase error is amplified using a PDI controller and operates a phase shifter in series with the rf supplying the cavity amplifiers (see Fig. 2). Two

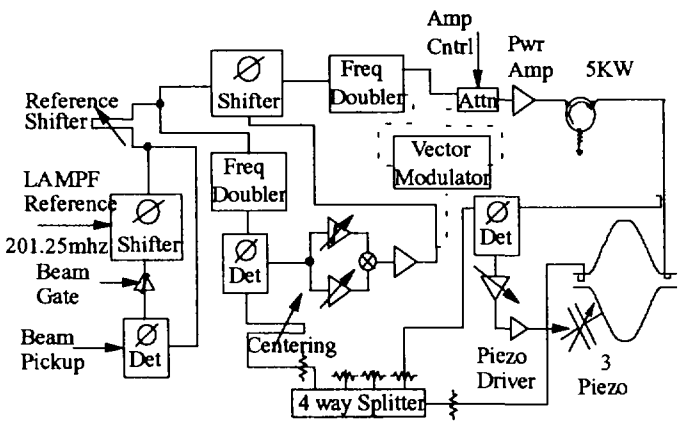

Fig 2. Control with drive from frequency reference.

different types of electronic phase shifters were tried in the controller. One was a Vector Modulator operating at 402.5 MHz. This unit has 3 dB amplitude modulation of the proper sign for amplitude control of the cavity in conjunction with 180^{o} of phase shift. The second shifter is a LAMPF designed shifter operating at 201.25 MHz. This analog shifter has 200 degrees of ultra-linear phase shift and less than one dB of amplitude change over the phase shift range. Comparisons of system performance between the two shifters showed the minimum phase error of 4 degrees and amplitude error of less than 2 percent achievable before loop instability were the same. As it turned out this mode was abandoned and neither of the shifters is used in the final operation.

Resonance Control

A phase comparison was made between the forward power from the final amplifier and the rf from the cavity-transmitted-pickup-probe to generate an error signal for resonance control of the cavity. This error signal was fed back by a proportional controller with a 60 Hz pole to the piezoelectric crystal drivers (see Fig. 2). The driver piezoelectric crystal combination has a pole at 140 Hz. This controller was intended to be a slow resonance controller and the mechanical lead screw tuners were to be used only to get the cavity within range of the crystals. The helium boil-off in the reservoir for the cavity causes a constant changing pressure on the cavity that results in a steady frequency change about a 100 Hz per minute. Depending on how well the refill system from the helium dewar is set, more than the entire 12 kHz range of the piezoelectric crystals is often used to keep the cavity on frequency. The piezoelectric frequency adjusters are necessary to operate the cavity, as the 5 kW amplifier could not drive the cavity when it is several kHz off resonance, even in the overcoupled condition.

D. Self Excited Mode

This mode was originally intended only for starting and conditioning the cavity. It consists of feeding the cavity transmitted pickup probe directly back to the amplifiers with phase adjustment and 30 dB of inter-loop rf gain, so the

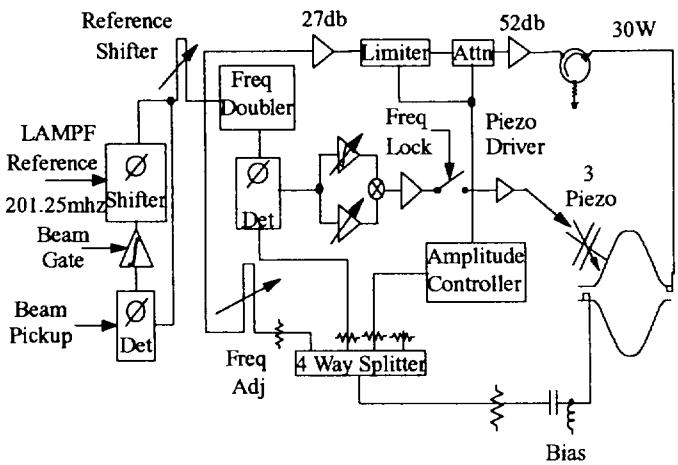

Fig 3. Control for the self oscillating mode.

system will self oscillate (see Fig. 3). It was included because of perceived ease of operation and was finally selected as the operating mode for the cavity for that reason. The frequency locking of the of cavity to the LAMPF beam is accomplished by using the piezoelectric crystals in a fast tuning loop with a Proportional-Integral controller. A phase lock to the beam frequency is also included. It consists of a phase comparison between a beam pickup and the cavity operating frequency that drives an electronic phase shifter in series with the reference phase shifter (see Fig. 3). This loop is to compensate for the reference 201.25 MHz timing signal phase drift due to several hundred feet of air dielectric cable that is not temperature controlled. This loop incorporates a sample and hold circuit for the error signal as the beam is pulsed. We use an Integral controller for this loop.

RESULTS

Operation of the system in its various modes and controller setups gave the same close loop response when operating at high loaded Q's (1 X 10^{9}). Due to the stiffness and mass of the cavity construction, microphonics have not

been much of a problem. The cavity is shock mounted on a stand attached to an isolated floor to reduce driving frequencies. The first mechanical resonance appears at 78 Hz and a thermo-acoustic resonance at 87 Hz is severe but intermittent. It may be related to the level of the helium in the reservoir. The driven mode was extremely difficult to operate. The slow response of the cavity when operating at high Q made aligning the cavity resonance to the operating frequency and locking the resonance control loop extremely difficult. It was necessary to use a spectrum analyzer with a noise floor of -120 dBm to find resonance. One tended to scan right through the resonance point before the cavity began to respond. With 1.6 MHz of tuning range to search, scanning slowly takes a prohibitively long time. One can adjust the trombones in the self excited loop and when the feedback is positive the cavity will start. The resonance can easily be set by observing reflected power from the cavity and is quite stable. By viewing the difference frequency from the phase control bridge, one can easily set the cavity to the null frequency with the mechanical tuner. A switch can close the control loop, locking the cavity to the reference frequency. The system has been operated in the LAMPF accelerator for two run cycles. The experimenters using the device have operated the system. Loop gains are set at the beginning of the cycle and have not required any service during the run. Coupling is set for critical coupling at the operating field level. We found that the cavity could be controlled at the high loaded-Q levels when we first turned on the system and the 5 kW amplifier has never been hooked up to the cavity. We operate with the 30 watt solid state pre-driver that will supply 6 MV/M accelerating fields at loaded-Q of 1 x 10^9. Operating with the low power amplifier limits the possible accidental X-ray level that could be generated, simplifying worst case accident scenarios. After the first run period, we increased loop rf gain to 30 dB from a few dB, to increase the turnon speed of the cavity. This was to eliminate switching back to the VCO mode to measure the cavity Q that required disconnecting and reconnecting some cables. With proper padding and the use of two control elements, the turnon overshoot was reduced but we could never eliminate it at the higher loop gains. Cables and couplers were calibrated and the experimental computer is used to take data on the forward and reflected power levels to calculate the Q with the overshoot occurring.

The system is extremely sensitive to noise introduced through the electronics. When closing the control loops, we were introducing 60 Hz noise into the system. Separating the dc power supply wires from the signal wires in the cable dressing for the bin helped this problem. We also found it necessary to move the power supply out of the bin because of magnetic pickup from its transformer. We still experience some performance degradation from 60 Hz pickup.

MICROPHONICS

We made a few measurements on the microphonics associated with the cavity using a digital scope with a fast Fourier transform. The scope could not contend with the frequency drift due to the helium boil off. I had to lightly lock the phase loop with the integral gain control to keep the cavity close to frequency during the time it took for the scope to accumulate enough data to generate an averaged spectrum. I measured the output of the phase detector comparing the cavity frequency with the LAMPF reference. Applying an inverse sign function to the ratio of bridge full output to measured spectrum gives the data reported in Fig. 4. The

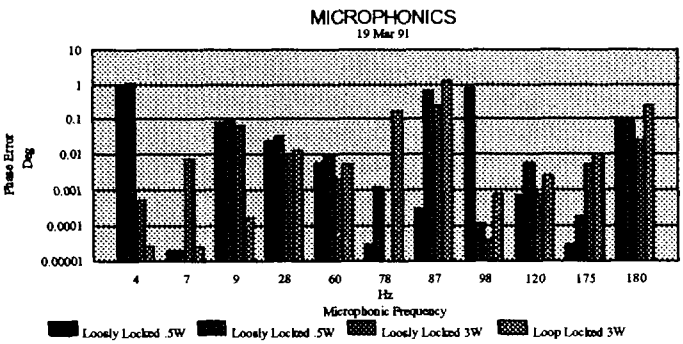

Fig 4. Phase Error due to Microphonic Vibrations.

loop is able to suppress the first three or four low frequency modes when it is tightened. Note that the 60 Hz components increase when the loop is tightened indicating that the 60 Hz is being introduced by the controller. The mechanical resonance at 78 Hz is spurious. The thermo-acoustic oscillations at 87 Hz occurred during part of the data taking for the Locked Loop spectrum. The loop does maintain lock when this oscillation occurs and may suppress it somewhat. The error due to this oscillation effects data being taken on the experiment although the original specification for control was 5 degrees in phase and 5 percent in amplitude. The experimenters correct for the pion beam energy shifts due to the phase changes by reading the loop phase error with the experiment computer.

REFERENCES

[1] J. M. O'Donnell, J. Davis, R. A. DeHaven, E. Gray, R. J. Johnson, R. E. Lomax et al., A Superconducting Radio Frequency Cavity for Manipulating the Phase Space of Pion Beams at LAMPF, Nuclear Instruments and Methods in Physics Research A317, July 1992, p. 445

IMAGE PROCESSING AND COMPUTER CONTROLS FOR VIDEO PROFILE DIAGNOSTIC SYSTEM IN THE GROUND TEST ACCELERATOR(GTA)*

Rozelle Wright, Mark Zander, Stan Brown, Darryl Sandoval, Doug Gilpatrick, Harold Gibson

Accelerator Technology Division, Los Alamos National Laboratory, Los Alamos, NM 87544

Abstract

This paper describes the application of video image processing to beam profile measurements on the Ground Test Accelerator (GTA). A diagnostic was needed to measure beam profiles in the intermediate matching section (IMS) between the radio-frequency quadrupole (RFQ) and the drift tube linac (DTL). Beam profiles are measured by injecting puffs of gas into the beam. The light emitted from the beam-gas interaction is captured and processed by a video image processing system, generating the beam profile data. A general purpose, modular and flexible video image processing system, *imagetool*, was used for the GTA image profile measurement. The development of both software and hardware for *imagetool* and its integration with the GTA control system (GTACS) will be discussed. The software includes specialized algorithms for analyzing data and calibrating the system. The underlying design philosophy of *imagetool* was tested by the experience of building and using the system, pointing the way for future improvements. The current status of the system will be illustrated by samples of experimental data.

Video Profile Monitor (VPM) Overview

The purpose of the video profile monitor is to measure horizontal and vertical beam profiles in GTA.[1,2] A secondary goal is to measure horizontal and vertical beam positions. The measurement takes place in the Intermediate Matching Section (IMS) located between the Radio Frequency Quadrapole (RFQ) and the Drift Tube Linac (DTL). The video system uses intensified video (TV) cameras to look at beam activated gas fluorescence. Basically we want to insert a camera in the beam line and take a picture from which we'll measure the beam's location and size. Since the amount of light produced is in relation to the number of particles interacting with the gas, this technique should be able to provide physical measurements of the beam as to size and shape. The concept seems simple but the implementation is not quite so straight forward.

Video System Configuration

The video system equipment configuration is shown in figure 1. It is located in three main places: the accelerator beam line, the racks, and the control room. Its use for diagnostics is described more fully in [2].

The accelerator beam line equipment consists of two computer controlled video cameras. Each camera has a controllable image intensifier and a motorized lens system which allows computer control of its focus, iris and zoom. They are pointed at a calibration light emitting diode(led). There is one camera situated to obtain images of vertical beam profiles and another situated to obtain images of horizontal beam profiles. A piezo electric valve is used to inject gas into the accelerator.

The racks contain electronics that interface the equipment on the accelerator to the computer control system. Video monitors, a video oscilloscope and manual controls are

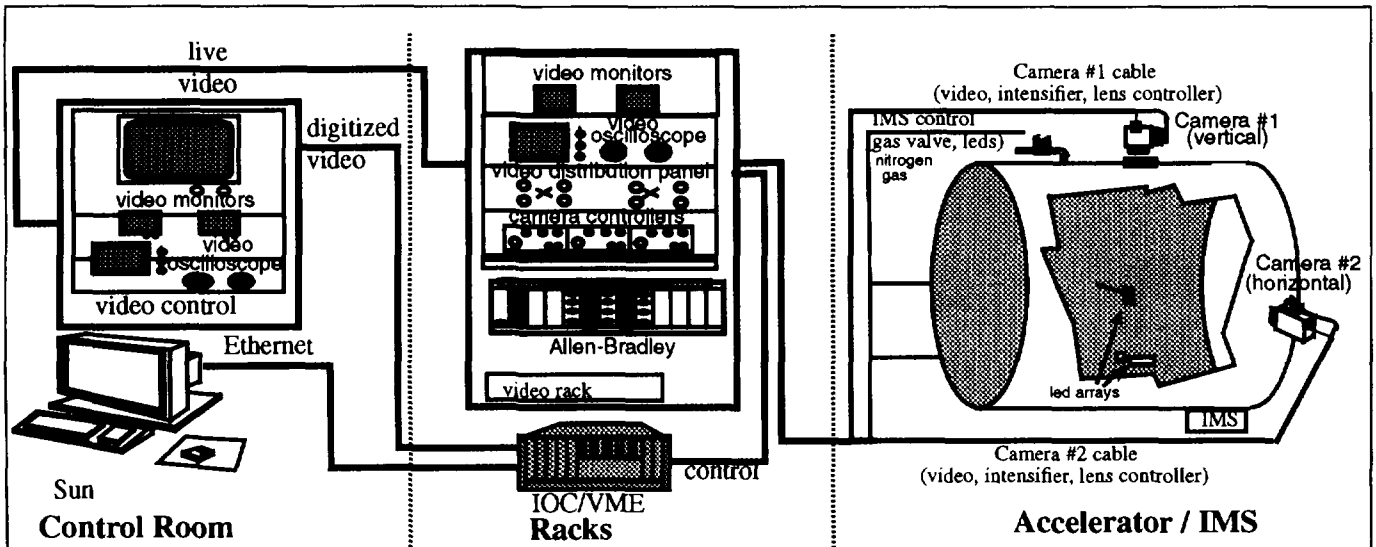

Fig. 1 Video Profile Monitor System

* Work supported and funded by the US Department of Defense, Army Strategic Defense Command, under the auspices of the US Department of Energy.

available for off-line testing of the equipment. An Allen Bradley interface and a VME based input output controller (IOC) supply the actual computer interfaces. In the VME crate are two video digitizers, two video memories and a video display unit all purchased from Datacube.

The control room uses Sun workstations as operator interfaces. These are connected to the rack equipment via ethernet. A display of the digitized video image is brought into the control room from the VME crate over a fiber optic link. Two video monitors display the analog data from each camera. A video oscilloscope is also available.

Video System Software

The video system software can be broken down into a number of distinct parts: basic hardware controls; video controls; real time plotting and analysis; and off-line analysis.

The software is distributed between the Sun and the IOC. The operator interface and off-line analysis execute on the Sun using OpenWindows and the Unix operating system. The control programs and real time programs for plotting and analysis execute on the IOC using the VxWorks (real time Unix) operating system. VxWorks executable subroutines to support the video hardware are provided by Datacube.

Off-line analysis is accomplished through a program, *imagetool* [3], which displays images and allows user written analysis codes to be invoked through menus. Initially *imagetool* also provided a menu driven operator interface which passed commands to VxWorks, via a remote shell interface, to invoke Datacube video subroutines. Figure 2 shows a typical image and plot generated by *imagetool*.

The GTA Control System (GTACS)[4] is used for control of the basic hardware including auxiliary video controls such as lens control, intensifier control, gas valve controls and video timing. GTACS applications are built with a set of

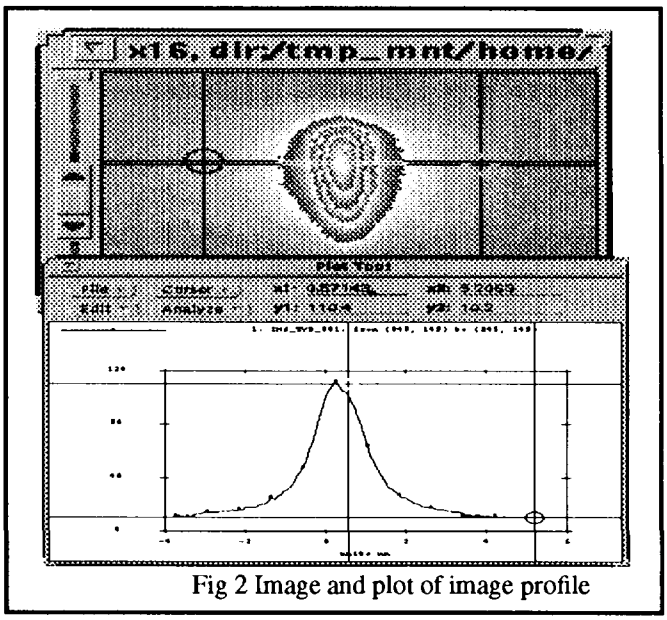

Fig 2 Image and plot of image profile

control system building tools which require very little programming. These tools worked very well for the simple controls and operator interface involved. Figure 3 shows the main video control screen generated by GTA.

The video controls themselves were more challenging, They were initially developed independently from GTACS. After the video controls were working well they were integrated with GTACS. This was done by using GTACS subroutine records and sequences to call datacube subroutines. The *imagetool* menus used for control were replaced by standard GTA operator screens.

The implementation of the real time plotting and analysis utilizes a hardware graphics overlay. This is used to plot a line or a column of image data which can be updated at

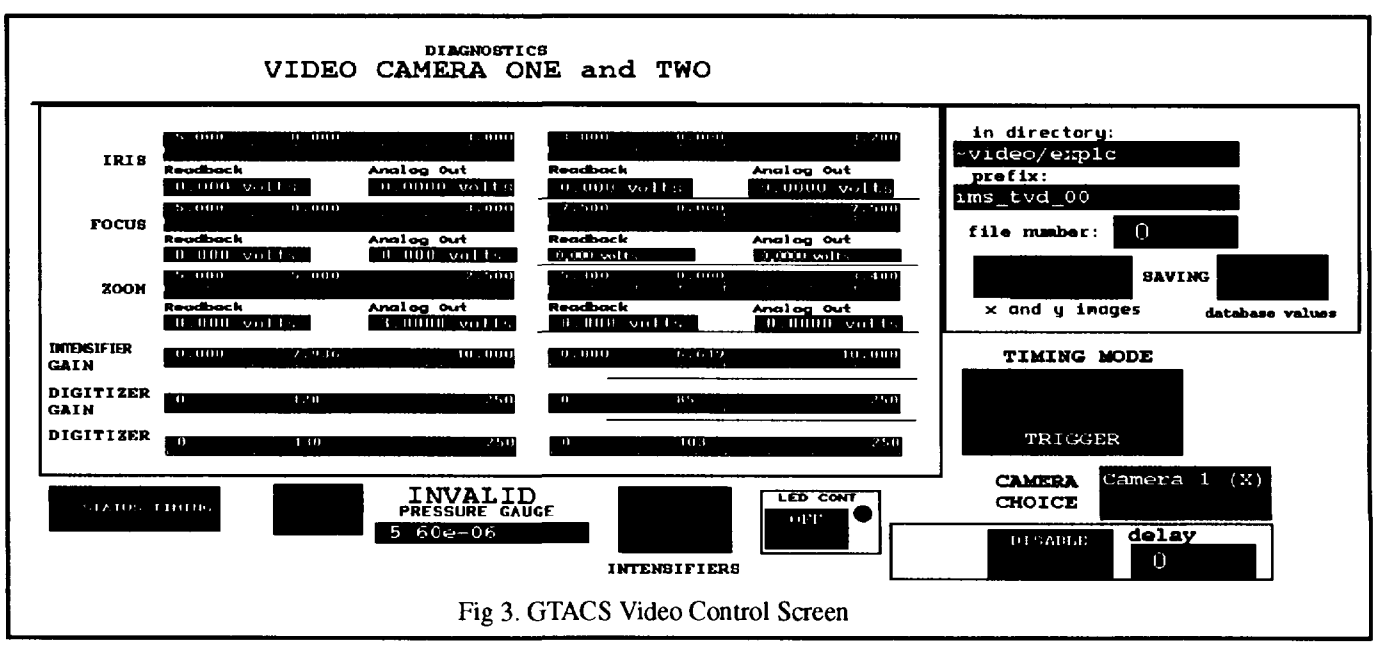

Fig 3. GTACS Video Control Screen

a rate of up to10 Hz. In addition, measurements such as full width half maximum may be printed on the plots.

Experience with System

It took some time before its operational characteristics were known. During this time of uncertainty, helium was used as the injected gas rather than nitrogen to prevent ice formation on the cryogenic RFQ. We are still learning about the system but some of the experiences to date are outlined below.

The first challenge was to find and correct major system problems that would prevent operation of the system. As an example of the problems encountered, an illegal set point caused the GTACS timing unit to generate a series of small pulses instead of one single pulse. Since this particular channel was connected to the gas valve, it repeatedly opened the valve causing a tank of gas to be emptied into the accelerator vacuum. To prevent recurrence of incidents of this type we now use a small reservoir to limit the amount of gas that can be dumped into the vacuum at one time. The GTACS system was also modified so that it would not respond disastrously to bad set points.

The first data collected indicated that the beam width was approximately the width of the accelerator beam pipe just up stream of the video profile monitor station. This beam width is much larger than expected. At this point we were confident that the gas valve subsystem was working correctly and we started using nitrogen as the injected gas. We also gated the image intensifier to integrate over no more than the duration of one macro pulse. After these adjustments were implemented the data began to give results which were closer to what was expected. A careful examination of the data led us to the hypothesis that the data was the sum of a broad low amplitude Gaussian and a narrower, high amplitude Gaussian. We have written software to fit two Gaussians of this type to the data. When the low amplitude fitted Gaussian is subtracted from the original data the resulting signal appears to be a reasonable representation of the beam with much flatter tails that the original.

Calibrating the system was also difficult. To obtain spatial calibrations a face plate with two columns of 4 holes each was put over an LED in the field of view of the camera. The exact location of the upper left hole was then measured. The idea was to turn on the LED and automatically find the position of each hole in the image. A simple code was written to find these points of light and calculate their centroids. In practice it was very difficult to take an image that would give sufficient contrast between the lights and the background. The light points were frequently of different intensities. To add to the problem, the focus of the lens was set to the beam position which was approximately 5 mm in front of the LEDs. As a result the points of light were out of focus. Despite the above problems, calibrations were successfully run and plots were made of the center of the lights to check the calibrations. Data was then taken with the calibration lights on to visually verify that the calibrations were being correctly applied to the beam data.

Future Directions

We shall continue to refine our data collection and analysis techniques so as to obtain useful data. As we gain experience we are discovering how best to operate the equipment. This will lead to more complete automation of the system for equipment operation as well as data collection.

Another improvement would provide calibrations that are more reliable and more easily obtained. This is still the hardest part of the process. The calibration procedure depends on automatically finding the calibration lights. If it fails to find the lights, it is not readily apparent to the operator what adjustments should be made to insure a better calibration. This is an open ended problem at present.

The final task is to integrate the results of the video profile monitor with the rest of the accelerator diagnostic data. When this is done the system will cease to be an interesting experiment and turn into a useful diagnostic.

Conclusions

We have successfully designed and implemented the controls for a video diagnostic system to measure beam profiles. Experience has shown us that even though the system is not straight forward to use, it is not too difficult to achieve reasonable results. In the future we hope to achieve a turnkey operation and demonstrate the usefulness of the diagnostic.

References

[1] Gilpatrick, Power, "RFQ and IMS Permanent Diagnostics", LA - UR # LA-CP-91-168 (Dec. 1990)

[2] D.P. Sandoval, R.C. Garcia, J.D. Gilpatrick, M.A. Shinas, R. Wright, V. Yuan and M.E. Zander, "Video Profile Diagnostic System for GTA", This Conference.

[3]]Mark E. Zander, "Imagetool: Image Processing on the Sun Workstation", SPIE Conference on Applications of Digital Image Processing 14, Vol. 1567, 9 (1991)

[4] A.J. Kozubal, D.M. Kerstiens, J.O. Hill and L.R. Dalesio ,"Run-time environment and application for the ground test accelerator control system", Nucl. Instr and Meth. 292 (1990)

PROGRESS ON A ONE GIGAWATT, ONE MICROSECOND PULSE LENGTH, HIGH CURRENT RELATIVISTIC KLYSTRON

M.V. Fazio, B.E. Carlsten, R.J. Faehl, W.B. Haynes, T.J.T. Kwan,
D.G. Rickel,R.M. Stringfield, R.F. Wasierski
Los Alamos National Laboratory, MS-H851, Los Alamos, NM 87545

Abstract

The development of a one gigawatt, high current relativistic klystron tube is underway for producing one microsecond long, 1.3 GHz microwave pulses at a 5 Hz pulse repetition frequency. This paper describes the theory, modeling, and experimental development of the microwave tube. The one microsecond pulse length is almost an order of magnitude beyond what has been achieved with a high current relativistic klystron. Achieving a peak power approaching 1 GW for 1 μs requires a stable electron beam on that time scale, and an optimized extraction efficiency in the output cavity. The microwave tube design was guided by theory and particle-in-cell code modeling that relate output cavity extraction efficiency to the amplitude of the beam harmonic current modulation and output cavity shunt impedance. Current experimental results are presented. The 1 MV, 10 kA, 1 μs pulse length, 5 Hz pulse-repetition-rate pulsed power modulator used to power the relativistic klystron is also described.

Theory and Modeling

In this section, we review basic relativistic klystron amplifier (RKA) physics. We show how the power extraction from the device depends on both the harmonic current content of the beam and also on its excess kinetic energy, which is the difference between the actual kinetic energy and the minimum required to transport the beam. As the beam is bunched, the kinetic energy is decreased, and there exists an optimum amount of bunching which leads to the maximum power extraction. For devices operating on time scales of 1 μs, the optimum harmonic current is only about 75%, leading to a dc-beam to microwave efficiency of less than 35%. The theory and modeling results, briefly summarized here, are treated much more extensively in references [1] and [2].

In our RKA, an annular, intense (5 kA), mildly relativistic (500 keV) electron beam passes through three cavities. The first cavity is externally driven and impresses an axial momentum variation on the initially uniform beam. Current modulation grows as the beam travels, as the momentum variation causes variations in the beam's axial density. We can describe the beam current in terms of its Fourier components

$$I(t,z) = I_0 + I_1(z)\cos(\omega t + \phi_1) + I_2(z)\cos(2\omega t + \phi_2) + \ldots .$$

The maximum harmonic current possible, for a delta function bunch of current, is twice the DC current. The fundamental current I_1 is typically around $1.4I_0$ for conventional klystrons. For an RKA, the harmonic content is usually $\leq 1.0I_0$. We must simultaneously maximize I_1 and extract the maximum kinetic energy from the beam in order to have the highest microwave power.

We wish to understand how $\Delta\gamma$, the maximum kinetic energy we can extract from the beam, depends on I_1. The amount of available energy is the difference between the injection energy (the depressed kinetic and potential energy) and the minimum injection energy (again summing the kinetic and potential energies) required to transport the bunched beam. Two effects are occurring as the beam is bunched and then decelerated in the output cavity. First, as the beam is bunched, the kinetic energy is depressed and the beam velocity decreases because more energy is required in the space-charge fields. Additional conversion from kinetic to potential energy is required in the output cavity as the bunch velocity is decreased further. As the bunched beam current is increased, we see that the kinetic energy available for extraction is decreased by both the larger potential depression requirement and by the larger minimum kinetic energy needed for transporting the higher current beam.

The largest permissible beam current, I_{max}, corresponds to a beam potential energy increase (and kinetic energy decrease) of

$$e\phi_b = \left(\gamma_{inj} - \gamma_{inj}^{\frac{1}{3}}\right) m_o c^2 \qquad \text{so}$$

$$I_{max} = \frac{2\pi\varepsilon_o m_o c^3}{e} \frac{\left(\gamma_{inj}^{\frac{2}{3}} - 1\right)^{\frac{3}{2}}}{\ln\frac{r_w}{r_b}} .$$

We see that the kinetic energy drop is not the injection voltage and that there is residual kinetic energy. One might think that since some kinetic energy remains, additional current can be pushed through the cylinder. However, removal of any additional kinetic energy drops the beam velocity v_o, which in turn increases the charge density and requires more increased potential energy from the beam than was given by the drop in the kinetic energy. This nonlinear slowing of the bunch as it forms aids its growth, and can be responsible for significant harmonic beam currents (greater than $1.0\ I_o$). If the beam current is near the threshold current I_{max}, and is increased slightly, a significant reduction in the beam's kinetic energy (and velocity) is possible. At the threshold current, a majority of the injection energy is partitioned into the potential energy fields; in Fig. 1 we see the partitioning of the total energy into kinetic and potential energy parts as a function of the injection gamma, γ_{inj}, and the beam current.

We can invoke energy conservation to calculate the minimum total beam energy for a given beam current. Solving for the minimum potential and kinetic energy gives

Work supported and funded jointly by the DoD Office of Munitions and the DOE Defense Programs through the joint DoD/DOE Munitions Technology Development Program, and by the Army Harry Diamond Laboratories and Missile Command.

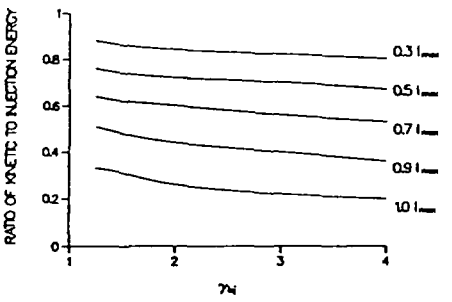

Fig. 1. Partitioning of injection energy for different injection energies and beam currents

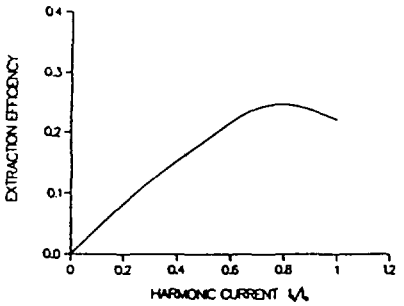

Fig. 2. Extraction efficiency versus harmonic current for a 500 kV, 5 kA beam with radius of 3.2 cm and wall radius of 3.65 cm. Best extraction is for 65% harmonic current.

$$\gamma_{min}^{\frac{2}{3}} = \left(\frac{PE + KE}{m_0c^2} + 1\right)^{\frac{2}{3}} = \left(\frac{I_{peak}}{8.5\text{ kA}} \ln\frac{r_w}{r_b}\right)^{\frac{2}{3}} + 1 \quad .$$

For a given peak current, I_{peak}, the difference between γ_{inj} and γ_{min} is the available kinetic energy for conversion to microwaves. The maximum power extraction possible is

$$P_{out,max} = \frac{1}{2} I_1 (511\text{ kV})(\gamma_{inj} - \gamma_{min}) \quad .$$

It is clear we want to simultaneously generate as much beam harmonic current as possible while minimizing γ_{min}. If the beam was collected by a conducting surface within the output cavity, this limitation would no longer be valid, since the beam's potential energy would be reconverted into kinetic energy. However, the plasma generated will become too large for microsecond pulse lengths.

Although a smaller beam radius leads to more harmonic current, we found that the maximum extraction occurs at the minimum beam-to-wall spacing possible. For a beam pipe radius of 3.65 cm and beam at 500 keV and 5 kA, the maximum extraction for a beam radius of 3.2 cm occurs with a harmonic current of 70% (dc beam to microwave efficiency of 25%), and for a beam radius of 3.4 cm with a harmonic current of 75% (efficiency of 30%). In both cases, beam harmonic current could easily exceed 100%. In Fig. 2 we plot extraction efficiency versus harmonic current for a 5 kA beam at a radius of 3.2 cm. We see that the maximum extraction, 25%, occurs at a fundamental current component of only 70%, far below the maximum current we can generate.

Experimental Tube Development

The first generation RKA has been constructed and operated on the BANSHEE pulsed power modulator. These results are described in detail elsewhere [3,4], but are briefly summarized here. The RKA design consists of a field emission diode producing a hollow beam that passes through the coaxial quarter-wave input cavity and idler cavity, and on to the rectangular waveguide output coupler placed transversely to the beam. The RKA drift pipe diameter is 7.3 cm. The rf drive to the input cavity is 5 kW and is coupled to the input cavity through a loop. The annular electron beam is supplied by a 6.35 cm-diameter circular stainless-steel field-emission cathode. Guiding of the electron beam is accomplished by a pulsed, strong uniform magnetic field (0.5 to 1.0 T) along the electron beam axis. For rf beam modulation measurements, a linear array of eleven B-dot loops were placed 5 cm apart along a section of drift pipe. Annular beam thickness is 2 to 4 mm.

Early RKA work produced a modulated electron beam for 1 μs with a peak rf current (I_1) of 1 kA and a voltage of 350 kV. Some experimental configurations produced beam modulation in excess of 2 μs which was the full width of the pulsed-power modulator pulse driving the RKA. The dc beam current was about 2.5-3 kA giving approximately a 30% beam modulation ($I_1/I_0 = 0.3$). The component of beam power at the microwave drive frequency (1.3 GHz) was approximately 175 MW. Approximately 50-70 MW was coupled into rectangular waveguide and gains of 20-40 dB were measured. The modulated-beam power to microwave output power coupling efficiency was ~30%. The low output coupling efficiency was due primarily to the inability to adjust the output gap tuning and shunt impedance.

A second generation RKA design, currently being tested [5], has incorporated the following three major design improvements: (1) The nominal input beam voltage and current produced from the field emission diode electron gun and transported through the RKA has been increased from 350 kV and 2.5 kA, to over 600 kV and 5 kA with a pulse duration of 1 μs. (2) A measurement of the output power dependence on input power level gave no hint of saturation up to the maximum available 5 kW drive level, indicating that a higher input drive would give a larger output power. A 500 kW magnetron source has replaced the 5 kW input drive amplifier previously used. (3) The theory and modeling indicate the sensitivity of output power on output gap shunt impedance, tuning, and Q. A new output cavity, described in reference [5], has been built with variable tuning, loading, and shunt impedance to allow adjustments of these parameters for optimal conversion efficiency of modulated-beam power to microwave output power.

A new input cavity was needed because the microwave input drive was increased from 5 kW to 500 kW by the installation of a high power magnetron. Power was coupled to the original cavity through a loop fed by 0.5 in coaxial cable. Since this scheme was inadequate for the new 500 kW power level, a new input cavity was designed that is fed through an iris by reduced-height rectangular waveguide. The stainless steel cavity is a quarter-wavelength coaxial line, shorted at one end and capacitively loaded by the gap at the other end. The loaded Q of the cavity, at low power without beam, was measured to be 20. The customary copper plating is unnecessary because the beam loading is

so heavy (cavity Q with full beam loading is ~10, compared to an unloaded Q of ~400) that resistive losses in the cavity walls are negligible compared to the power absorbed by the beam. This is seen by comparing the beam impedance, which is 2000 to 4000 ohms, to the cavity shunt impedance which is around 100,000 ohms. Since the magnetron driver must be matched to the cavity at full beam loading for efficient power transfer, the cavity, without beam, had to be strongly overcoupled to the magnetron. This condition results in a VSWR (looking into the cavity from the input waveguide) of 27 without beam. The VSWR approaches 1 with full beam loading.

Figs. 3 and 4 show the beam current pulse overlaid with the magnetron reflected power and the modulated beam current envelope 25 cm downstream from the input cavity gap. The salient features that should be noted are that: 1) the reflected magnetron power goes to zero as the beam current increases from zero indicating good coupling to the beam loaded cavity, 2) the rf pulse length of the modulated beam is about 2.5 μs, and 3) the rf current on the beam is about 8% with 60 kW of rf drive. Only about 5% modulation is needed from the first cavity for the RKA to operate as we have designed it.

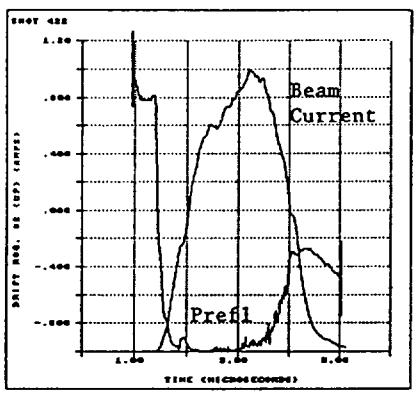

Fig. 3. Beam current overlaid on magnetron reflected power signal showing how the impedance change due to beam loading leads to a matched condition between the input waveguide and the input cavity. (Scale on vertical axis is arbitrary.) Peak beam current is 4.5 kA.

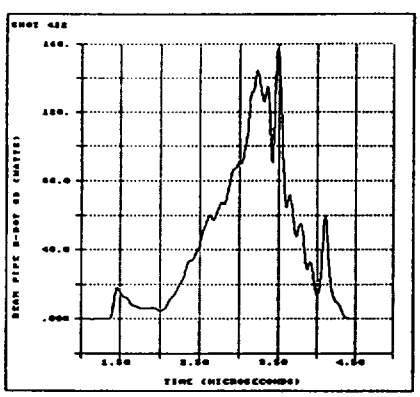

Fig. 4. Detected signal from B-dot loop located 25 cm downsteam from the input cavity gap. This B-dot loop measures the 1.3 GHz current modulation on the beam. The rf modulation imparted to the beam by the input cavity with 60 kW of input power is about 8% or I_1/I_0 = 0.08.

Repetitively Pulsed Modulator Development

BANSHEE is the repetitively pulsed, high voltage modulator used to produce a high current relativistic electron beam for high power microwave tube development at microsecond pulse lengths. The design goal for BANSHEE is to achieve a 1 MV, 10 kA pulse, with a 1 μs flat-top, driving a load impedance in the range of 100 Ω at a pulse repetition frequency of 5 Hz. The long term goal is a prf of 100 Hz. With BANSHEE, thyratron-switched line-type modulator technology is being extended to the megavolt and multi-kiloampere level. Performance to date has achieved 600 kV at 6 kA for 1 μs at a 1 Hz prf [6]. A prf of 5 Hz at 600 kV and 5 kA has been also been achieved for 60,000 shots. The successful operation of two state-of-the-art high power thyratrons in parallel, at a voltage, current, and pulse length appropriate for 1 μs, repetitive-pulse development of the RKA has been demonstrated.

Summary

We have described our RKA experimental results and our second generation RKA design that is currently being tested. We have added to the understanding of RKA physics with the importance of the role of intense space charge in limiting the efficiency of the device because of the beam potential depression that reduces the kinetic energy available for conversion to microwaves. We have produced a stable 650 kV, 5 kA annular beam of microsecond duration from an explosive field emission cathode. Repetitively pulsed, 1 μs pulse-length RKA operation is possible because of the capability of the BANSHEE thyratron-switched line-type modulator. Rep-rate RKA development awaits the availability of a dc magnet for beam transport through the klystron.

References

[1] B.E. Carlsten, M.V. Fazio, R.J. Faehl, T.J.T. Kwan, D.G. Rickel, R.M. Stringfield, "Theory and modeling of a relativistic klystron amplifier with high space charge for microsecond applications," Proc. SPIE 92 Intense Microwave and Particle Beams III, Los Angeles, Ca., Jan. 1992, **1629**, p. 57-68.

[2] B.E. Carlsten, R.J. Faehl, M.V. Fazio, T.J.T. Kwan, D.G. Rickel, R.D. Ryne, R.M. Stringfield, "Effect Of Intense Space Charge In Relativistic Klystron Amplifiers," Proc. 9th Intl. Conf. on High Power Particle Beams, Washington, D.C., May 1992, to be published.

[3] D.G. Rickel, M.V. Fazio, B.E. Carlsten, R.J. Faehl, T.J.T. Kwan, R.M. Stringfield, "Experimental Progress on a Microsecond Pulse-Length Relativistic Klystron Amplifier," Proc. SPIE 92 Intense Microwave and Particle Beams III, Los Angeles, Ca., Jan. 1992, **1629**, p. 51-56.

[4] D.G. Rickel, , M.V. Fazio, B.E. Carlsten, R.J. Faehl, T.J.T. Kwan, R.M. Stringfield, R.F. Wasierski, "Development of a Long-Pulse 1.3 GHz Relativistic Klystron Amplifier," IEEE Trans. on Plasma Science Special Issue on High Power Microwave Generation, vol. 20, no.3, June 1992, p 373-382.

[5] M.V. Fazio, et al. "The Experimental and Theoretical Development of a One Gigawatt, Repetitively Pulsed, One Microsecond Pulse Length, High Current Relativistic Klystron and Modulator," Proc. 9th Intl. Conf. on High Power Particle Beams, Washington, D.C., May 1992, to be published.

[6] R.M. Stringfield, et al. "The Development of a One Microsecond Pulse-Length, Repetitively Pulsed, High Power Modulator and a Long Pulse Electron Beam Diode For the Production of Intense Microwaves," Proc. 9th Intl. Conf. on High Power Particle Beams, Washington, D.C., May 1992, to be published.

RF SYSTEM DESCRIPTION FOR THE GROUND TEST ACCELERATOR RADIO-FREQUENCY QUADRUPOLE*

Amy H. Regan, Donna Brittain, Daniel E. Rees, and Christopher D. Ziomek
Los Alamos National Laboratory
Los Alamos, NM 87545

Abstract

This paper describes the RF system being used to provide RF power and to control the cavity field for the ground test accelerator (GTA) radio-frequency quadrupole (RFQ). The RF system consists of a low-level RF (LLRF) control system, and RF Reference Generation subsystem, and a tetrode as a high-power amplifier (HPA) that can deliver up to 300 kW of peak power to the RFQ cavity at a 2% duty factor. The LLRF control system implements in-phase and quadrature (I&Q) control to maintain the cavity field within tolerances of 0.5% in amplitude and 0.5° in phase in the presence of beam-induced instabilities.

Figure 1 is a simplified block diagram depicting the major components required to provide a stable RF field inside the accelerating cavity. This paper describes the identified components and presents measured performance data. The user interface with the systems is described, and cavity field measurements are included.

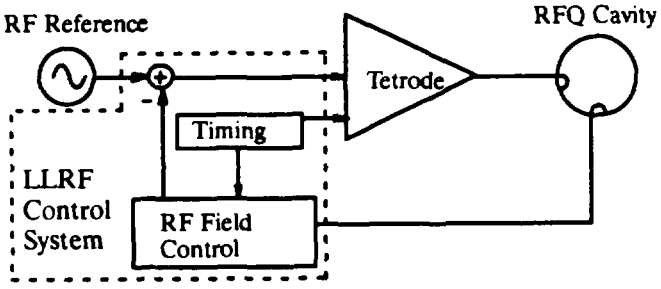

Fig. 1 RF system block diagram.

RF Reference

The RF reference generation subsystem provides coherent, phase-stable signals to each cavity field-control subsystem of the GTA. The reference output signal is low-noise and extremely phase-stable. Figure 2 is a measurement of the RF Reference output spectrum to the LLRF control system.

LLRF Control System

In actuality the LLRF control system performs four separate functions: cavity field control, timing distribution, diagnostic monitoring, and cavity resonance detection. In order to maintain a stable RF field in the cavity, the first two functions are mandatory. These will be discussed.

*Work supported and funded by the US Department of Defense, Army Strategic Defense Command, under the auspices of the US Department of Energy.

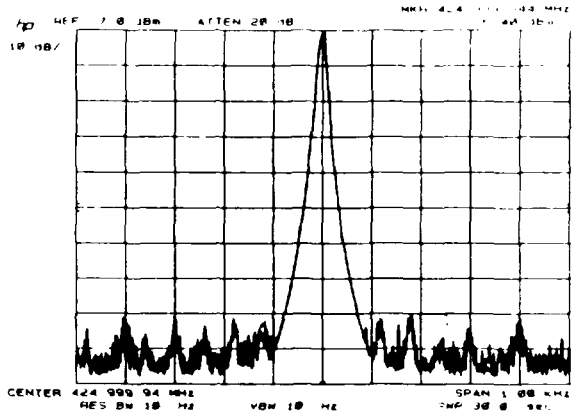

Fig. 2 RF reference spectrum input to feedback loop.

RF Field Control

The field control subsystem regulates the RF field inside the RFQ cavity in the presence of external disturbances by implementing PID-feedback control. This is done by comparing a sample of the accelerating RF field to the input RF reference signal, downconverting this signal to baseband and then resolving it into its in-phase and quadrature components. These I and Q components undergo PID control simultaneously in parallel circuits. The modified components are the control outputs used to modulate the baseband signal. This modulated signal is upconverted to form the LLRF output signal that drives the high-power amplifier. Figure 3 is a functional block diagram of the field control subsystem, whose performance specifications are as follows:

LLRF output (max.)	+ 18 dBm
Steady-state phase error of cavity RF field (max.)	±0.5 elec. degrees
Steady-state amplitude error of cavity RF field (max.)	±0.5%
Response time of LLRF system (max.)	2 μs

The cavity field control system is packaged in the modular VXIbus architecture. Individual VXI modules perform the various functions depicted in Figure 3.

Calibration and setup of the field control subsystem must occur before the accelerator can be operated and whenever accelerator hardware is replaced or modified. Two calibration procedures exist. The first is performed to adjust the phase of the cavity field signal. Due to different electrical lengths of cabling and different devices in the cavity field control subsystem, the cavity field sample has an arbitrary phase rotation. By varying the arbitrary phase shift through the software and observing its effect on test points in the hardware, the phase shift required to produce proper I/Q re-

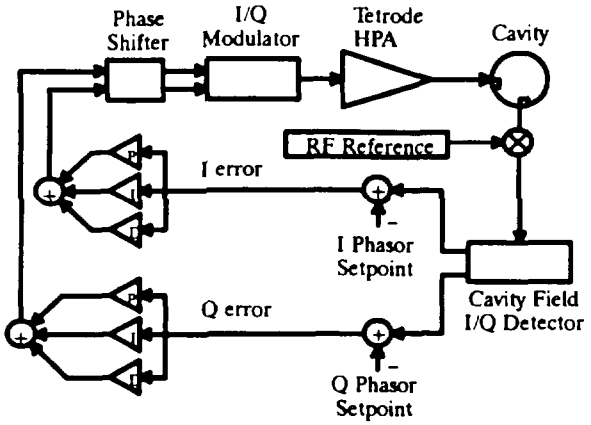

Fig. 3 Functional block diagram of cavity field control system.

lationships is obtained. This phase shift differs with operating setpoint, so a table of proper phase set points is experimentally determined.

The second setup procedure that must take place is the creation of a gain-scheduling table. All of the gains, setpoints, and initial conditions in the control system can be altered by the operator. The gain-schedule table provides data for an interpolation algorithm that automatically calculates these control parameters for any given operating setpoint and is created prior to accelerator operation. This table accounts for any non-linearities within the cavity-fill sequence and within the tetrode amplifier. Creation of the gain-scheduling table requires manual experimentation by an expert user in order to determine proper field control parameters for various operating setpoints. As the parameters are adjusted and determined, the control software enters them into the gain-scheduling table. Again, this procedure involves both interfacing with the hardware through VXI module front panel test points and use of the control software via a workstation.

Timing

The GTA requires synchronous clocks and triggers for the various components of the RF system. These signals are generated within the timing subsystem and are distributed throughout the components. Each field control VXI module incorporates these signals locally, in circuitry based primarily upon the Analog Devices Am9513A system timing controller. The properties of each internal timing signal can be modified through the software. In addition, some modules transmit external timing signals. For example, the HPA RF gate is specified by the operator and is transmitted via a fiber optic cable to the tetrode amplifier. This gate provides an operating window for the HPA driver.

High-Power Tetrode Amplifier

The high-power tetrode amplifier is a three-stage amplifier designed to deliver up to 300 kW of RF power at 425 MHz to the RFQ for 2-ms pulse durations at pulse repetition rates up to 10 Hz. The amplifier consists of an 800-W solid-state driver, which has approximately 45 dB of gain, followed by an air-cooled, 14-kW triode cavity amplifier and a water-cooled Burle 4616 tetrode amplifier, which has a gain of approximately 20 dB and an average anode dissipation of approximately 30 kW. In the GTA application the water-cooled tetrode is operated so that the pulsed saturated output power is approximately 350 kW. However, in short-pulse applications (100 μs), an output of up to 700 kW of peak power has been achieved from the same amplifier architecture with only a 20% change in operating condition and slight cavity modifications. Table 1 includes the operating conditions for the final stage of the tetrode amplifie.

Table 1

Burle 4616 Tetrode Operating Conditions

DC Plate Voltage	19.000 V
DC Screen Voltage	1800 V
Grid Bias	-300 V
DC Plate Current	25.8 A
DC Screen Current	1.0 A
DC Grid Current	.04 A
DC Cathode Current	26.84 A
Fundamental Peak Plate Current	43.3 A
Fundamental Peak Cathode Current	45.3 A
Peak Plate Swing	14.000 V
Peak Grid Swing	300 V
Peak Plate Dissipation	178.1 kW
Peak Screen Dissipation	1800 W
Peak Output Power	300 kW

Figures 4 and 5 represent data taken from some of the latest measurements from the amplifier development for the Superconducting Supercollider. The operating conditions for these measurements differ from those described above in that the anode voltage is 25 kV, the screen voltage is 2200 V, the dc and fundamental current levels are higher due to a higher drive level, and the operating frequency is 427.6 MHz. Figure 4 shows the power transfer characteristic of the amplifier. Note that the input/output characteristics are linear over the range of interest (0–300 kW). This is achieved by operating the first stage class A. The second stage is also operated class A through the use of cathode modulation. The final stage is operated class AB. Figure 5 shows the bandwidth of the amplifier, illustrating a 3-dB bandwidth of approximately 1 MHz at 427.6 MHz.

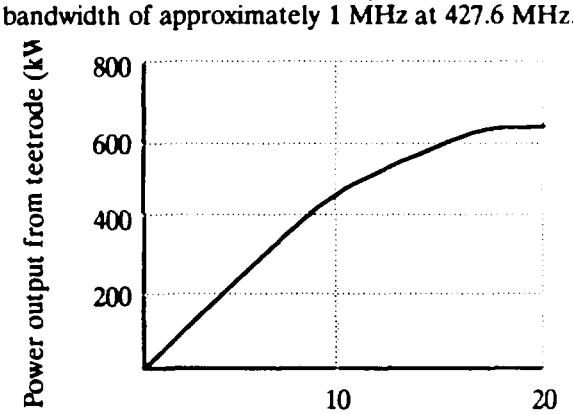

Fig. 4 Amplifier power transfer characteristics.

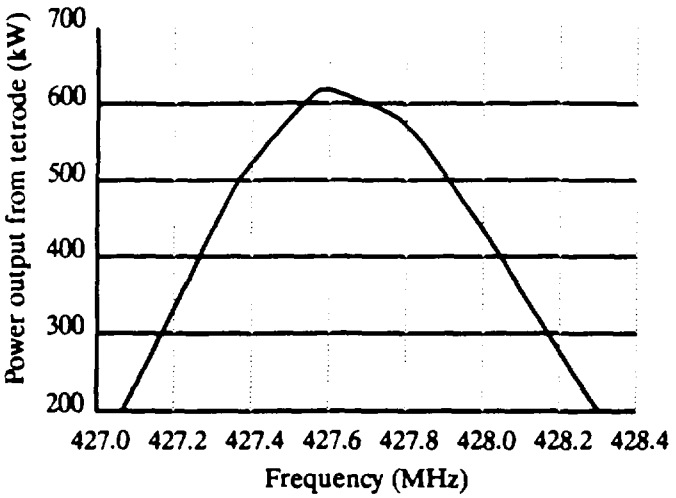

Fig. 5 Amplifier bandwidth.

User Interface

No input from the operator is required for RF Reference during accelerator operation. However, the subsystem does perform self-diagnosis throughout operation and notifies the operator should something fail. For example, the output frequency and power level are constantly monitored and compared to allowable operating ranges. The operator is notified only should these values fall outside of the permissible ranges.

A remote SUN workstation serves as the primary user interface for operating the LLRF and high-power tetrode amplifier systems. The remote operator can turn the systems on/off and control operating parameters. Actual equipment control for the RF subsystems is performed by the local processor resident in each system. Figure 6 shows the relationship between the local area network (LAN) and the RF subsystem processors

The high-power tetrode amplifier system is also locally operable. It is equipped with an Allen Bradley (AB) programmable logic controller, which provides the sequencing of startup, fault and status monitoring, and sequencing of the shutdown of the amplifier equipment. (The user can initiate startup/shutdown of the amplifier system by means of front-panel push buttons when it is in local operating mode.) The local processor is connected through fiber optic cable to a VME-based AB scanner module. The scanner makes portions of the AB processor memory accessible over the VME bus. A VME-based processor and an Ethernet card provide the link to the remote workstation for remote-mode monitoring and operation of the high-power amplifier system.

System Performance Data

When the LLRF, HPA, and control systems were installed and integrated, a series of tests was undertaken to verify that the entire system met the defined specifications. Figures 7 and 8 show measurements of the RFQ RF field I and Q components during operation under closed-loop control with the particle beam present during the pulse. The

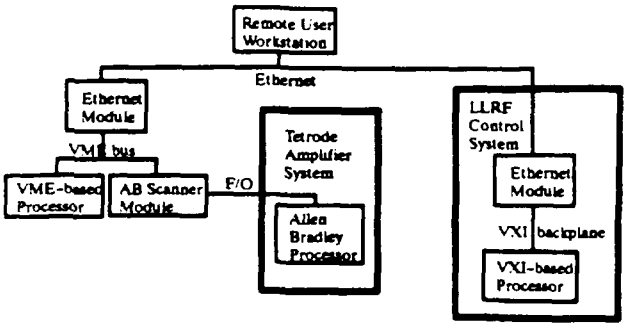

Fig. 6 User interface configuration.

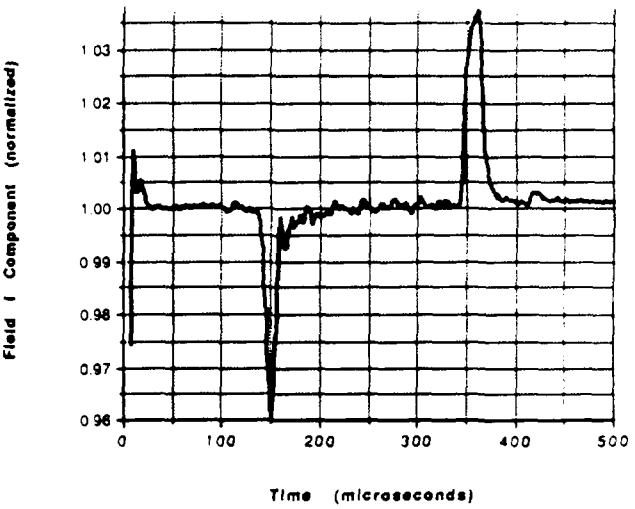

Fig. 7 RFQ cavity field I component during RF pulse.

points where the beam is turned on and off are apparent, as is the level of stability achieved during the beam pulse. The data show performance well-within the 0.5% amplitude and 0.5° phase error budgets.

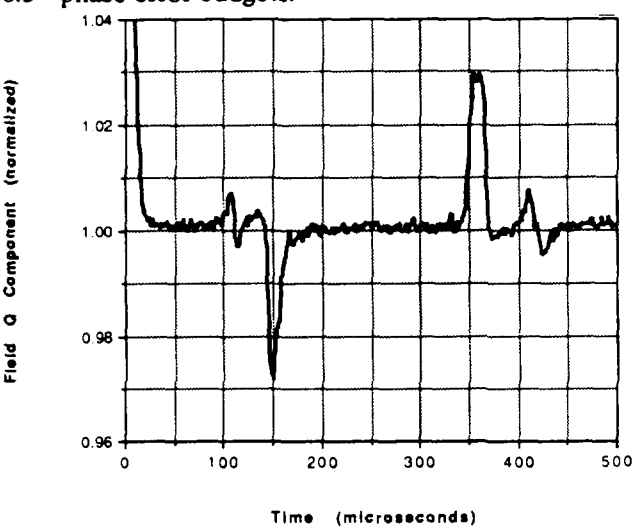

Fig. 8 RFQ cavity field Q component during RF pulse.

Acknowledgments

The authors wish to recognize G.O. Bolme, R. Cole, R. Graybill, D. Kerstiens, S.P. Jachim, J. Power, S. Ruggles, and O.R. Sander for their valuable contributions to this paper.